Design for material properties of additively manufactured metals using topology optimization

Mishra, Vibhas; Ayas, Can; Langelaar, Matthijs

DOI
10.1016/j.matdes.2023.112388

Publication date
2023

Document Version
Final published version

Published in
Materials and Design

Citation (APA)
Mishra, V., Ayas, C., & Langelaar, M. (2023). Design for material properties of additively manufactured metals using topology optimization. *Materials and Design*, *235*, Article 112388. https://doi.org/10.1016/j.matdes.2023.112388

Materials & Design 235 (2023) 112388

Contents lists available at ScienceDirect

Materials & Design

journal homepage: www.elsevier.com/locate/matdes

Design for material properties of additively manufactured metals using topology optimization

Vibhas Mishra *, Can Ayas, Matthijs Langelaar

Mechanical, Maritime and Materials Engineering, Delft University of Technology, Mekelweg 2, Delft, 2628CD, Zuid Holland, the Netherlands

ARTICLE INFO

Keywords:
Topology optimization
Microstructure
Additive Manufacturing
Cooling rate control
Property optimization
HSLA steel

ABSTRACT

In metal Additive Manufacturing (AM), the deposited material is subjected to a series of heating and cooling cycles. The locally occurring temperature extremes and cooling rates determine solid-state phase fractions, material microstructure, texture, and ultimately the local material properties. As the shape of a part determines the local thermal history during AM, this offers an opportunity to influence these material properties through design. In this paper, we present a way to obtain desired properties by controlling the local thermal history. This is achieved through topology optimization of the printed part while considering its entire transient thermal history. As an example of this approach, this work focuses on high strength low alloy steels, where resulting phase fractions significantly influence mechanical properties such as yield strength and ductility. These solid-state phase fractions depend on cooling rates in a particular critical temperature range. The phase composition and hence the local yield strength in target regions can be controlled by constraining the cooling time in this range. Numerical examples illustrate the capability of the proposed approach in adapting part designs to achieve various desired material properties.

1. Introduction

Metal Additive Manufacturing (AM) processes encompass a wide range of technologies in which the part is manufactured through sequential addition of the molten material, generally in a layer-by-layer manner, with the help of a heat source. Currently, functional metal parts with dimensions ranging from millimeters to several meters can be realized through various metal AM processes from various alloys such as titanium alloys, nickel based alloys, aluminum alloys, and steels [1]. For example, small parts with intricate details can be realized by Laser Powder Bed fusion (LPBF) processes. In contrast, large-scale parts with dimensions of a few meters can be manufactured by Directed Energy Deposition (DED) processes such as Wire and Arc Additive Manufacturing (WAAM).

The main advantage of AM technologies is that geometrically complex shapes can be realized which is not feasible with conventional manufacturing technologies such as milling and casting. To exploit this form freedom, Topology Optimization (TO) is often used in conjunction with AM. TO is a computational design tool through which the optimal geometric layout of a part is obtained to enhance parts specific performance. The designs obtained by TO tend to be geometrically complex and thus can often only be realized by AM [2].

The mechanical properties of a part depend on the microstructure development during the manufacturing process. In addition to this, the microstructure development is related to the thermal history experienced by the part during the process. The microstructure of metal has multiple aspects such as grain or cell size, grain morphology, crystallographic texture, and types and phase fractions of solid-state phases. When the molten metal is deposited, the thermal gradients and solidification rates in the melt zone determine the grain size and morphology [3]. For instance, the grain size in austenitic stainless steels depends on the solidification rate. A high solidification rate can be achieved by increasing the scan speed in the LPBF process which results in fine grain size [4]. Similarly, fine grain sizes are observed in the aluminum alloy (AlSi10Mg) struts manufactured by LPBF process [5], and the stainless steel parts manufactured by WAAM when they are subjected to high solidification rates [6,7]. In addition, the crystallographic texture also depends on the maximum heat flow directions and crystallographic texture of the already deposited material [1,8]. The type of solid-state phase transformations depends on the cooling rate experienced by the material after the solidification of the metal in a critical temperature range [9]. For example, in HSLA steels, the parent high-temperature FCC austenite phase transforms to child solid-states phases during cool-

* Corresponding author.
E-mail address: v.mishra@tudelft.nl (V. Mishra).

https://doi.org/10.1016/j.matdes.2023.112388
Received 23 March 2023; Received in revised form 28 September 2023; Accepted 4 October 2023
Available online 11 October 2023

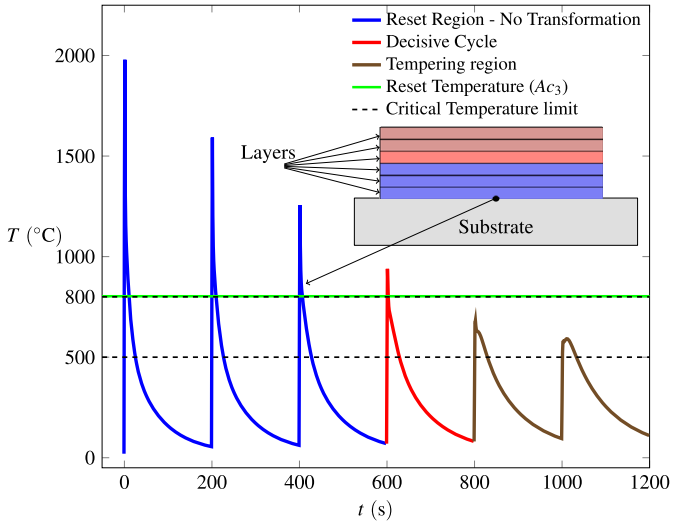

Fig. 1. The complete thermal history experienced by a material point during deposition of the layers in a layer-by-layer manner in an Additive Manufacturing process. The colors of the transient thermal history correspond to the color of the deposited layer.

ing by two competing phase transformation processes. Either through diffusive transformation into BCC ferrite or by the displacive transformation into the harder martensite phase reminiscent of solid-state phase transformations in Ti-6AL-4V [10–12]- another alloy widely used in AM. However, for nickel-based alloy (IN718) the microstructure heterogeneity that can be induced by the thermal cycles of AM is linked to precipitation and chemical segregation [13]. During WAAM of HSLA steels, the cooling time spent between the critical temperature range from 800°C to 500°C, determines the phase fraction of individual solid-state phases [14–18]. In this work, the focus is on WAAM-manufactured HSLA steel structures and control of the material specific solid-state phase transformations through design optimization. The extension of the presented approach for other alloys is out of the scope of the current paper but is briefly discussed in Section 6.

The right combination of phase fractions is essential for the mechanical performance of the produced parts. In HSLA steels when the cooling rate in the critical temperature range is low, the microstructure is dominated by phases with high ductility and low strength and vice versa. In the WAAM process, the thermal history experienced by a material region can be influenced by the local design features around that region. This also opens up the possibility to control the cooling rates in a material region or, an alternate representation of cooling rates, cooling time in the critical temperature range. Consequently, solid-state phase fractions can be controlled in a material region through appropriate design changes. In this paper, we consider that WAAM process parameters are fixed. The effect of the process parameters of the WAAM process on the resultant thermal history for HSLA has been thoroughly discussed in [18]. This implies for WAAM, a relation holds between the design, thermal history, and resultant yield strength distribution. In this work, this relation is used to locally obtain desired material properties from WAAM process through TO.

The solid-state phase fractions are dictated by the thermal history that can be predicted with a WAAM process simulation. Only a few studies have considered transient thermal simulation within TO. However, none of these studies can control the solid-state phase fractions. For instance, maximum temperature minimization over time has been investigated in [19]. Moreover, to facilitate heat transfer in the AM process, transient thermal compliance is minimized [20]. Our aim in this paper is to present a novel TO methodology to control the cooling time in local design regions. Consequently, we will be able to generate the part design to obtain a desired mechanical property distribution for the first time through computational design.

It remains to establish the relation between the thermal history of a material point and the microstructure development. Due to the sequential deposition of layers in WAAM process, deposited material experiences multiple heating and cooling cycles as shown in Fig. 1. The first heating and cooling cycle corresponds to its own deposition with a peak temperature above the melting point, which is approximately 1500 °C for steels. The subsequent cycles are due to the deposition of successive layers on the pre-deposited material. The peak temperatures observed in these subsequent cycles gradually decrease but can still be substantially high. During cooling in a material-specific critical temperature range, the parent solid-state phase transforms into child phases, e.g., in HSLA steels the austenite phase transforms into ferrite, bainite, and martensite [9]. The subsequent heating cycle and the corresponding peak temperature determine whether these child phases transform back to the parent austenite phase. In steels, the critical Ac_3 temperature is the temperature above which all child phases transform back to the parent phase completely [21,22,18]. This critical temperature is hence termed the reset temperature in the remainder and is indicated in Fig. 1. Consequently, the complete thermal history of a material point can be divided into three parts [18]. The first part is the reset region where the parent phase transforms into the child phases but then the child phases completely transform back into the parent phase during the subsequent heating. After the reset region, comes the decisive cycle in which the parent phase transforms to the child solid-state phases for the last time. The time spent by the material during cooling, in the critical temperature range for the decisive cycle determines the solid-state child phase fractions. Controlling this particular cooling rate through design changes would allow us to control the solid-state phase transformations, and therefore an important aspect of the metal microstructure, during the WAAM process. The thermal cycles after the decisive cooling cycle are the tempering cycles when the martensite phase if present, transforms to tempered martensite [9]. The effect of tempering is currently excluded from this study for simplicity since this is a second-order effect but the methodology developed can be extended to account for the tempering effects.

To evaluate the thermal history during WAAM, we consider a simplified, finite element-based process model to reduce the computational cost to a level that allows its integration into the TO process. Consequently, material properties are idealized as temperature-independent. Moreover, the material addition is considered in a layer-by-layer manner. This implies the finite elements associated with the deposited material are activated in a sequential manner in time. In line with the material deposition heat is added to the entire layer simultaneously for

a particular period and thereafter the part is allowed to cool. Melting and solidification of the metal are not included because during these phenomena temperature remains unchanged and the energy absorption during melting is balanced by energy dissipation during solidification [23]. Moreover, convective/radiative heat transfer through the part is neglected because conduction remains the dominant mode of the heat transfer method in WAAM processes [24]. By employing these simplifications we sacrifice the resolution related to the movement of the heat source, but achieve large gains in computational efficiency with limited loss of accuracy. Even with these simplifications, performing a topology optimization including a transient WAAM process simulation remains a computationally demanding task. For this reason, 3D examples are presently not feasible in our implementation, and instead, 2D numerical examples are studied. As a means to study the effectiveness of the method, these are nevertheless deemed adequate. In our numerical examples, we consider a WAAM process but the methodology remains valid for other metal AM processes such as LPBF. The cooling rates observed in LPBF process are higher compared to WAAM and thus require a corresponding transient thermal model with a higher temporal resolution.

A density-based TO framework is used for the design optimization [25]. The design is evaluated by solving the compliance minimization problem described in Section 2. We consider the WAAM of the compliance-minimized design. The thermal history of the compliance minimized design is evaluated by the simplified WAAM process model, detailed in Section 3. The relation between the cooling time and the resultant yield strength (σ_y) is also given in Section 3. We employ gradient-based optimization, which requires the sensitivities of the cooling time in the critical temperature range with respect to design variables. Therefore, the evaluation of the cooling time spent in the critical temperature range is formulated in a continuous and differentiable manner. This is done by applying combinations of smooth Heaviside functions, details of which are given in Section 4. Moreover, as discussed earlier, during the WAAM process the decisive cycle dictates the resulting solid-state phase of a material point. To account for this, weights are associated with each heating and cooling cycle. The weight is substantial for the decisive cycle whereas negligible for other cycles. The weighting functions used to emphasize the decisive cycle are detailed in Section 4 together with the novel optimization problem considered in this work. As discussed previously that the computational cost to include complete thermal history in TO is very high. In Section 5 the computational cost to evaluate the thermal history of a 2D TO design is given. Moreover, optimized designs obtained by various 2D numerical examples are also presented in Section 5. The conclusions drawn from this study and directions for future work are outlined in Section 6.

2. Minimum compliance TO problem

We first introduce a common TO problem, i.e., compliance minimization. The problem description is as follows:

$$\min_{\rho} \quad c = \frac{1}{2}\sum_{\Omega_M} \mathbf{u}_e^{\mathrm{T}}\mathbf{k}_e(\rho_e)\mathbf{u}_e, \tag{1}$$

$$\text{s.t.} \quad \mathbb{K}\mathbf{u} = \mathbf{f}. \tag{2}$$

$$V(\rho) \le V_0. \tag{3}$$

$$0 \le \rho_e \le 1, \quad \forall e \in \Omega_M. \tag{4}$$

Here, c is the compliance of the structure in the design domain Ω_M discretized with a structured mesh comprising bilinear finite elements. The array of design variables ρ_e, where $e = 1, \dots, M$ denotes the element number for a total of M elements, is represented by ρ. Nodal displacement degrees of freedom and the stiffness matrix of a finite element are represented by $\mathbf{u}_e$ and $\mathbf{k}_e$, respectively. Element stiffness matrices depend on the design variable ρ_e through the commonly used modified SIMP interpolation [25] scheme:

Table 1
Default Parameters for the optimization.

Modeling and Material Properties		Optimization parameters	
Element size	1 mm × 1 mm	p	3
Element Type	Plane stress Q4	Move limit	0.2
E_0	210 GPa	V_0	0.6 Ω_M
$E_{\min}$	$10^{-9}E_0$	Initial state	$\rho_e = 0.6\ \forall e \in \Omega_M$
Poisson's ratio (ν)	0.3	Stopping crit.	$\|\|\Delta\rho\|\|_\infty \le 0.01$
Domain thickness	1 mm	$r_{\min}$	2.5 mm
Thermal Properties			
κ_0	45 W/m °C	$\kappa_{\min}$	$10^{-9}\kappa_0$
c_{p_0}	496 J/kg °C	$c_{p_{\min}}$	$10^{-3}c_{p_0}$
ρ_m	7800 kg/m^3		

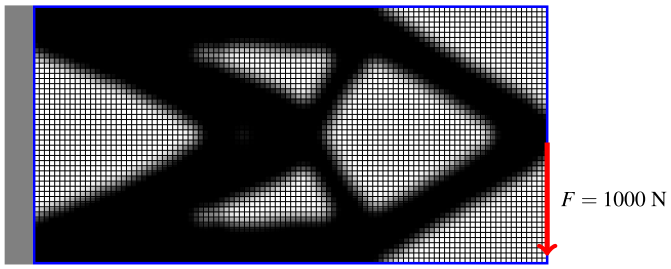

Fig. 2. Cantilever Beam Problem: The blue rectangular domain (50 mm × 100 mm) is the design domain, discretized with a structured mesh of bilinear quad elements. The displacements at the left boundary of the domain are fixed and a point load is applied indicated with a red arrow. The dark layout is the design obtained from compliance minimization.

$$E_e(\tilde{\rho}_e) = E_{\min} + \tilde{\rho}_e^p(E_0 - E_{\min}). \tag{5}$$

Here, Young's Modulus of the void and material is given by $E_{\min}$ and E_0, respectively. Young's Modulus is penalized with penalization exponent $p = 3$. E_e is Young's Modulus of an element e with filtered design variable $\tilde{\rho}_e$. Filtering is applied to density variables ρ to avoid the formation of checkerboard patterns in the design layout and to ensure a minimum feature size in the optimized structure. Filtered densities are given as follows:

$$\tilde{\rho}_e = \frac{\sum_{i\in\Omega_e^{\min}} w_i(\mathbf{x}_i)v_i\rho_i}{\sum_{i\in\Omega_e^{\min}} w_i(\mathbf{x}_i)v_i}, \tag{6}$$

$$w_i(\mathbf{x}_i) = r_{\min} - ||\mathbf{x}_i - \mathbf{x}_e||. \tag{7}$$

Eq. (6) defines the density filter applied to the design variable ρ_e at position $\mathbf{x}_e$ with element volume v_i [26]. Eq. (7) represents the weight (w_i) associated with the element i at $\mathbf{x}_i$ for the density filter. $\Omega_e^{\min}$ is the circular region with a radius $r_{\min}$ in which the filter is effective. $\mathbb{K}$, $\mathbf{u}$, and $\mathbf{f}$ are the global stiffness matrix, nodal degrees of freedom, and nodal loads, respectively. Eq. (3) represents the constraint on material volume $V(\rho)$. The allowed material volume in the design domain is V_0. Eq. (4) represents the bounds on the design variables. The gradient-based optimization algorithm Method of Moving Asymptotes (MMA) [27] is used.

As a test problem, a cantilever loadcase is considered. The loading and boundary conditions of the cantilever problem and the optimal design are given in Fig. 2. The material constants and parameters used for optimization are given in Table 1.

3. AM process model and process dependent properties

3.1. Simplified process model

To simulate the AM of the compliance-optimized design, we first fix the building direction. Based on the build direction, the complete design is discretized to L layers which are sequentially deposited in a

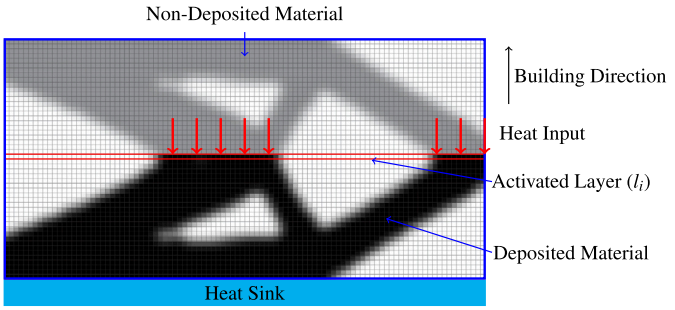

Fig. 3. Illustration of the simplified process model on the compliance optimized design layout. The cyan region indicates the heat sink condition to simulate the presence of the substrate. Based on the building direction, the complete deposition process is discretized into process intervals. In each process interval, the elements comprising the layer (l_i) are activated at once as shown in the red rectangle. The heat added to the deposited layer is indicated by the red arrows. The heating and subsequent cooling is simulated for each process interval to evaluate the thermal history.

total time of τ. A layer is represented by l_i, where $i = 1, \ldots, L$. Layer l_i is deposited, as shown in Fig. 3, in a process interval $(\tau_{l_{i-1}}, \tau_{l_i})$ at once.[1]

Recall that, to every deposited layer, a heat load is applied for a specific period of time, and then the layer is allowed to cool. The amount of heat added to the deposited layer is determined by the process parameters of the AM process. In WAAM, metal wire is melted with an electric arc and deposited. The geometry of the electric arc depends on the wire feed rate and travel speed of the arc. The material point is heated for the time period the electric arc requires to traverse itself. This is the duration, $\Delta\tau^{\mathfrak{h}}$, the heat load is applied to a newly deposited layer in the simplified process model. The duration $\Delta\tau^{\mathfrak{h}}$ is calculated by the ratio of the electric arc length in the deposition direction to the travel speed of the electric arc. These parameters are chosen from literature [18]. The length of the electric arc in the deposition direction is 12.9 mm and the travel speed of the electric arc is 8 mm/s. Since the heating time $\Delta\tau^{\mathfrak{h}}$ is kept constant for all the layers, layer l_i, is heated from $\tau_{l_{i-1}}$ to $\tau^{\mathfrak{h}}_{l_i}$, where $\tau^{\mathfrak{h}}_{l_i} - \tau_{l_{i-1}} = \Delta\tau^{\mathfrak{h}}$ and thereafter allowed to cool from $\tau^{\mathfrak{h}}_{l_i}$ to τ_{l_i}.

The following transient heat conduction equation:

$$\mathbf{C}_{l_i}(\rho)\dot{\mathbf{T}}_{l_i} + \mathbf{K}_{l_i}(\rho)\mathbf{T}_{l_i} = \mathbf{Q}_{l_i}(\rho), \qquad \text{if,} \quad \tau_{l_{i-1}} \le t \le \tau_{l_i}, \tag{8}$$

$$\mathbf{T}_{l_i} = \mathbf{T}_0, \qquad \text{at,} \quad t = \tau_{l_{i-1}}, \tag{9}$$

is then solved to evaluate the thermal history after the deposition of layer l_i. Here, $\mathbf{C}_{l_i}$ and $\mathbf{K}_{l_i}$ are the heat capacity matrix and thermal conductivity matrix after the deposition of layer l_i, respectively. $\mathbf{T}_0$ is the array of ambient temperatures at which the deposition process starts. $\mathbf{T}_{l_i}$ is the array of nodal temperatures and $\dot{\mathbf{T}}_{l_i}$ is its time derivative. The subscript l_i denotes that the nodal values are calculated when layer l_i, is deposited. The $\mathbf{Q}_{l_i}$ is the nodal heat load applied during the deposition of layer l_i. The amount of heat added to the elements in the process model is calculated by the power of the WAAM process. To calculate the heat load for a process interval, the power per unit volume (q_0) is associated with each activated element of the layer l_i. This power density is then scaled by the design variable associated with the element using the SIMP penalization as follows:

$$q_e = \tilde{\rho}_e^p q_0. \tag{10}$$

q_e is the power density associated with the activated elements and penalized with the density variable. The penalized power density is then integrated over the top edge of the activated element and assembled into the nodal heat load array. The nodal heat load is applied as follows

$$\mathbf{Q}_{l_i}(\rho) = \begin{cases} \mathbf{Q}_{l_i}(\rho) & \text{if,} \quad \tau_{l_{i-1}} \le t < \tau^{\mathfrak{h}}_{l_i} \\ \mathbf{0} & \text{if,} \quad \tau^{\mathfrak{h}}_{l_i} \le t \le \tau_{l_i}. \end{cases} \tag{11}$$

Eq. (9) represents the initial condition at the start of a process interval assuming the pre-deposited part cools down to ambient temperature before the deposition of the subsequent layer starts. This particular assumption is realistic for WAAM since, the size of a part is typically 2-3 orders of magnitude larger than the electric arc size. Therefore sufficient cooling time is available during subsequent layer deposition.

The thermal conductivity and heat capacity matrices are dependent on the design variables as follows:

$$\kappa_e(\tilde{\rho}_e) = \kappa_{\min} + \tilde{\rho}_e^{p_\kappa}(\kappa_0 - \kappa_{\min}), \tag{12}$$

$$c_{p_e}(\tilde{\rho}_e) = c_{p_{\min}} + \tilde{\rho}_e^{p_{c_p}}(c_{p_0} - c_{p_{\min}}). \tag{13}$$

Here, κ_e and c_{p_e} are the thermal conductivity and specific heat capacity of element e. $\kappa_{\min}$ and κ_0 are the thermal conductivity of void and material, respectively. Similarly, $c_{p_{\min}}$ and c_{p_0} are the specific heat capacity of void and material, respectively. The positive penalization exponents on the thermal conductivity and specific heat capacity are p_κ and p_{c_p}, respectively. For the considered heat conduction problem, the cooling rates are governed by the thermal diffusivity, which is given for an element e is given as follows:

$$\alpha_e = \frac{\kappa_e}{\rho_m c_{p_e}}. \tag{14}$$

Here, ρ_m is the physical density of the material which is constant. Substituting Eq. (12) and Eq. (13) in Eq. (14), and simplifying we get:

$$\alpha_e = \alpha_0 \left(\frac{\kappa_{\min}/\kappa_0 + \tilde{\rho}_e^{p_\kappa}(1 - \kappa_{\min}/\kappa_0)}{c_{p_{\min}}/c_{p_0} + \tilde{\rho}_e^{p_{c_p}}(1 - c_{p_{\min}}/c_{p_0})} \right). \tag{15}$$

Here, $\alpha_0 = \kappa_0/(\rho_m c_{p_0})$. If $p_\kappa = p_{c_p} \neq 0$, $\kappa_{\min}/\kappa_0 = 10^{-9}$ and $c_{p_{\min}}/c_{p_0} = 10^{-9}$, then $\alpha_e = \alpha_0$. This means that heat transfer through the void is possible which is physically incorrect. Therefore, we choose $p_\kappa > p_{c_p}$, to make thermal diffusivity design dependent. For $p_\kappa = 3$ and $p_{c_p} = 2$, thermal diffusivity will be linearly dependent on the design variable [20]. However, for $\tilde{\rho}_e = 0$ with $p_\kappa = 3$ and $p_{c_p} = 2$, $\alpha_e = \alpha_0 \left(\frac{\kappa_{\min}}{\kappa_0}\right) / \left(\frac{c_{p_{\min}}}{c_{p_0}}\right)$. Therefore, for $\kappa_{\min}/\kappa_0 = 10^{-9}$ and $c_{p_{\min}}/c_{p_0} = 10^{-9}$, $\alpha_e = \alpha_0$. Again the thermal diffusivity for the void and solid becomes indistinguishable. To circumvent this issue, $\kappa_{\min}/\kappa_0 = 10^{-9}$ and $c_{p_{\min}}/c_{p_0} = 10^{-3}$ are chosen. Through these selected parameters, the thermal diffusivity of the void becomes $10^{-6}\alpha_0$, and heat transfer through the void regions is effectively suppressed.

To solve the transient state equation given by Eq. (8), a Backward Euler Scheme is employed in the temporal domain. The motivation to choose this particular scheme is its unconditional stability for linear transient heat conduction problems [32]. The time step used to solve the state equation is chosen sufficiently coarse so that optimization can be realized in a reasonable computational time. The effect of time steps is studied in Section 5.1. Even though the time step is kept large the solution time might be high due to number of degrees of freedom. Therefore, a relatively coarse structured mesh of 100×50 bilinear quadrilateral elements is chosen for the optimization problem. Note that high-fidelity thermal models can be used to simulate the transient thermal history during the AM process. However, the additional computational costs make the optimization problem computationally intractable.

3.2. Relation between cooling time and yield strength

The relation between the cooling time, hardness, and yield strength (σ_y) is shown in Fig. 4. The relation between the cooling time in the

[1] Note that manufacturing of a design through AM is considered even though the design has problematic overhanging features. Our main focus is to control local thermal history through design optimization. For controlling overhangs in a design several other methods are already present in literature [28–31].

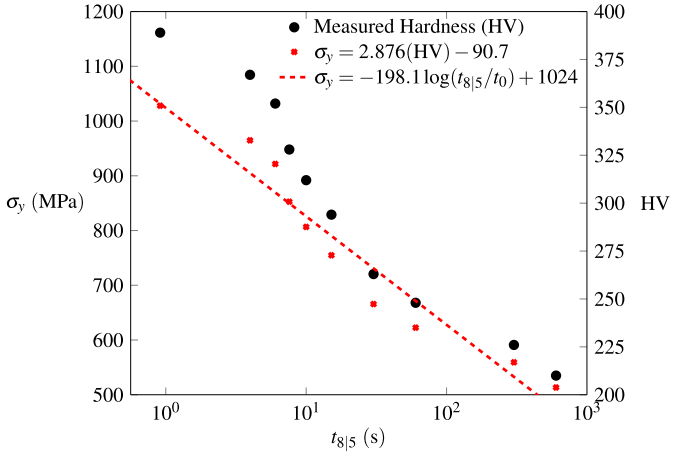

Fig. 4. Correlation in the cooling time between the critical temperature range 800 °C to 500 °C, measured Vickers Hardness (HV), and correlated Yield Strength (σ_y).

critical temperature range and the Vickers Hardness is given in [18]. In Fig. 4, the horizontal $t_{8|5}$-axis represents the cooling time between 800 °C to 500 °C, and black data points represent the measured Vickers Hardness (HV). The yield strength is calculated using the empirical relation

$$\sigma_y = 2.876(\mathrm{HV}) - 90.7 \tag{16}$$

suggested by [33]. σ_y can be directly correlated to the cooling time spent in the critical temperature range 800 °C to 500 °C through linear regression as:

$$\sigma_y = -198.1 \log\left(t_{8|5}/t_0\right) + 1024. \tag{17}$$

Here, $t_0 = 1$ s, is a constant to introduce unitless quantity $t_{8|5}/t_0$ before the logarithmic operation is applied.

4. Cooling time estimation and full optimization problem

4.1. Cooling time spent in the critical temperature range

We denote the upper and lower bounds of the critical temperature range as $\bar{T}$ and $\underline{T}$, respectively. For HSLA steels, the critical temperature range is between $\bar{T} = 800$ °C and $\underline{T} = 500$ °C. A typical thermal history for a node of the compliance minimized cantilever design (see Fig. 2) obtained by our simplified process simulation is shown in Fig. 5. The thermal history of the node has multiple heating and cooling cycles. The first cycle represents the deposition of the layer in which the node indicated by red is activated. The subsequent heating and cooling cycles represent the deposition of the consecutive layers above the node. Each finite element node in the design (apart from the topmost layer) experiences a similar thermal history with multiple heating and cooling cycles. A robust strategy is required to evaluate the cooling time of the decisive cooling cycle.

The entire thermal history of the node n is given by $T_n(t)$. The temperature history of the node n activated at the deposition of layer l_i, after deposition of layer l_j, is represented with ${}^{l_i}_{l_j}T_n(t)$. Here, the index $j = i, \ldots, L$. ${}^{l_i}_{l_j}T_n(t)$ represents the thermal history of the node n activated in the interval $(\tau_{l_{i-1}}, \tau_{l_i})$, during the process interval $(\tau_{l_{j-1}}, \tau_{l_j})$. A combination of Heaviside functions can be used to evaluate the time spent in the critical temperature range in a particular process interval. For a layer l_j deposited after layer l_i, the time spent in the critical temperature range by node n in the process interval $(\tau_{l_{j-1}}, \tau_{l_j})$ is evaluated as:

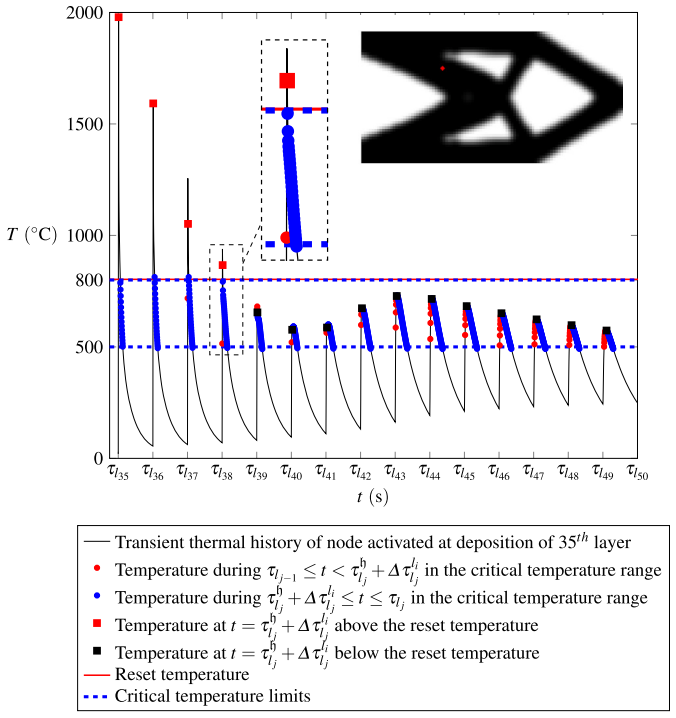

Fig. 5. Transient thermal history of a node represented by the red in the compliance minimized design obtained by process simulation.

$$ {}^{l_i}_{l_j}\mathbf{t}_n = \int_{\tau_{l_{j-1}}}^{\tau_{l_j}} \bar{H}\left({}^{l_i}_{l_j}T_n(t)\right) \underline{H}\left({}^{l_i}_{l_j}T_n(t)\right) dt, \tag{18}$$

$$\text{with,} \quad \bar{H}\left(T(t)\right) = \frac{1}{1 + \exp\left(\dfrac{-k_W(\bar{T} - T(t))}{\bar{T}}\right)}, \tag{19}$$

$$\underline{H}\left(T(t)\right) = \frac{1}{1 + \exp\left(\dfrac{-k_W(T(t) - \underline{T})}{\underline{T}}\right)}. \tag{20}$$

The parameter k_W determines the shape of the Heaviside functions, when combined together act as a window function that extracts the time interval where the temperature is in the critical temperature range $[\underline{T}, \bar{T}]$. The effect of the parameter k_W is shown in Fig. 6, for the temperature range 500 °C to 800 °C. The function $\bar{H}(T)\underline{H}(T) \approx 0$ everywhere except $500\,°\mathrm{C} \le T \le 800\,°\mathrm{C}$ where $\bar{H}(T)\underline{H}(T) \approx 1$. For $k_W = 100$, this behavior is captured with the desired accuracy as shown in Fig. 6. Therefore $k_W = 100$ is chosen in this study. Differentiable, smooth Heaviside approximations are essential in order to allow gradient-based optimization.

For the thermal history shown in Fig. 5, the data points labeled with red and blue circles are identified to be within the critical temperature range with $\bar{H}(T)\underline{H}(T) > 0.1$. Note that Eq. (18) accounts for the time the node spends in the critical temperature range during both heating and cooling. However, only the cooling phase is relevant for the final microstructure development. In order to isolate the time spent during the cooling phase, the time spent during the heating phase should be excluded. It means that for a heating-cooling cycle, the time spent in the critical temperature range for the data points before the peak temperature should be discarded. For this purpose, the estimation of the time instance at which the peak temperature occurs becomes crucial. The time at which the peak temperature occurs for the node n activated during the deposition of layer l_i, during the deposition of l_j has two aspects:

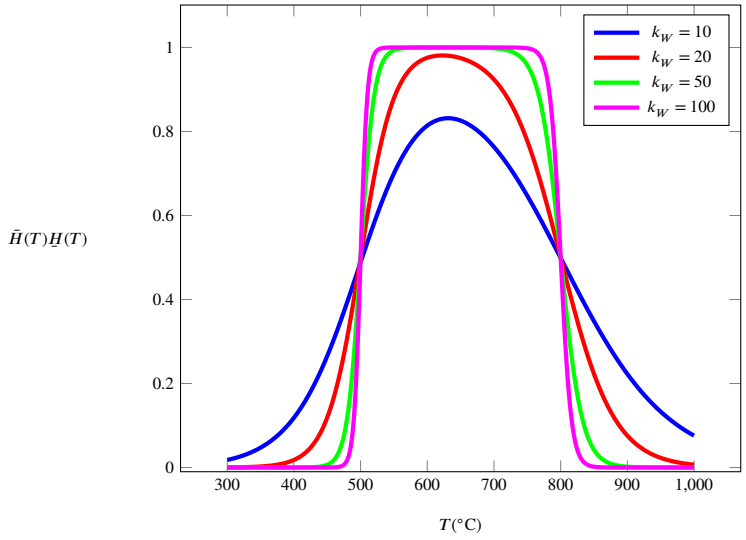

Fig. 6. The effect of parameter k_W on the combination of Heaviside functions to extract the total time spent in the critical temperature range 800°C to 500°C.

1. The duration of heating. In this period heat is added, and thus temperature is expected to rise.
2. The time the heat is conducted from layer l_j to node n activated during the deposition of l_i.

An additional Heaviside function, ${}^{l_i}_{l_j}H_n(t)$, is introduced for the node n activated at layer l_i, which is used to filter out the time spent during heating while layer l_j is deposited:

$$ {}^{l_i}_{l_j}H_n(t) = \begin{cases} 0, & \text{if,} \quad \tau_{l_{j-1}} \le t < \tau^{\mathfrak{h}}_{l_j} + \Delta\tau^{l_i}_{l_j} \\ 1, & \text{if,} \quad \tau^{\mathfrak{h}}_{l_j} + \Delta\tau^{l_i}_{l_j} \le t \le \tau_{l_j}. \end{cases} \tag{21} $$

Note that the exact Heaviside function is used here since this operation is not design-dependent and consequently is not a part of the sensitivity calculation. Here, $\Delta\tau^{l_i}_{l_j}$ is the time delay required for the heat to diffuse through conduction and reach node n when layer l_j is deposited. This time delay is estimated as

$$ \Delta\tau^{l_i}_{l_j} = \frac{\left(\Delta L^{l_i}_{l_j}\right)^2}{\alpha_0}. \tag{22} $$

Here, $\Delta L^{l_i}_{l_j}$ is shortest path between layer l_j and node n. This shortest path is design-dependent. During optimization, the design is subject to change in every iteration hence the conduction path is unknown. Therefore, it is complicated to estimate $\Delta L^{l_i}_{l_j}$. For simplicity, it is taken

$$ \Delta L^{l_i}_{l_j} = (j - i + 1)\Delta x. \tag{23} $$

Here, Δx represents the height of the element which is equivalent to layer thickness shown in Fig. 3. Since the optimization starts with a uniform gray design, i.e. $\rho_e = V_0$, and the heat equation (Eq. (8)) is scaled by the design variable, the assumption holds valid during the initial optimization iterations. When the optimized design converges to a black-and-white design the assumption does not hold valid. However, it is observed that by using Eq. (22) the time instances at which temperature peaks occur can be approximated reasonably well. For the thermal history shown in Fig. 5, square-shaped red markers represent the temperature at $t = \tau^{\mathfrak{h}}_{l_j} + \Delta\tau^{l_i}_{l_j}$ which captures the temperature peaks at the desired level of accuracy. The time spent by node n in the critical temperature range during cooling, after the layer l_j is deposited is then given as

$$ {}^{l_i}_{l_j}\tilde{\mathfrak{t}}_n = \int_{\tau_{l_{j-1}}}^{\tau_{l_j}} \left({}^{l_i}_{l_j}H_n(t)\right) \bar{H}\left({}^{l_i}_{l_j}T_n(t)\right) \underline{H}\left({}^{l_i}_{l_j}T_n(t)\right) dt. \tag{24} $$

In Fig. 5, the temperature data in the critical temperature range during heating and cooling is represented by red and blue colored circles, respectively. It can be observed in Fig. 5 that through this approach the time corresponding to heating in the critical temperature range is filtered out. Note that, if $j \approx i$, the heating of node n happens at a much higher rate compared to the cooling, therefore time contribution from the heating phase is negligible. However, if $j >> i$ the heating of node n happens at a slightly slower rate. Therefore a time contribution from the heating phase would be more notable. Still, distant layer additions are not likely to become a decisive cooling cycle that dictates the material microstructure.

4.2. Identifying the decisive process interval

The previous section showed that the time spent in the critical temperature range can be calculated through a continuous function in each process interval. Recall that, a decisive cooling cycle dictates the final solid-state phases. Therefore, the cooling time during the decisive process interval should be determined.

To identify the decisive process interval, weights are assigned to each process interval. For the thermal history shown in Fig. 5, the cooling time of the fourth cooling cycle is crucial. This is because it is the last process interval where temperatures exceed the reset temperature. The assignment of the weight has two aspects:

1. Determine the process intervals in which the temperature exceeds the reset temperature with a reset weight.
2. From process intervals that are identified with temperatures above reset temperature, extract the last one with a sequential weight.

Recall that the temperatures at $t = \tau^{\mathfrak{h}}_{l_j} + \Delta\tau^{l_i}_{l_j}$ have been observed to approximate the peak temperatures reasonably well. Therefore, in order to identify the process intervals with peak temperatures above the reset temperature, the temperature, ${}^{l_i}_{l_j}\mathrm{T}_n$, at $t = \tau^{\mathfrak{h}}_{l_j} + \Delta\tau^{l_i}_{l_j}$ is extracted from the thermal history. The following smooth Heaviside function is introduced to compute a reset weight depending on this extracted peak temperature:

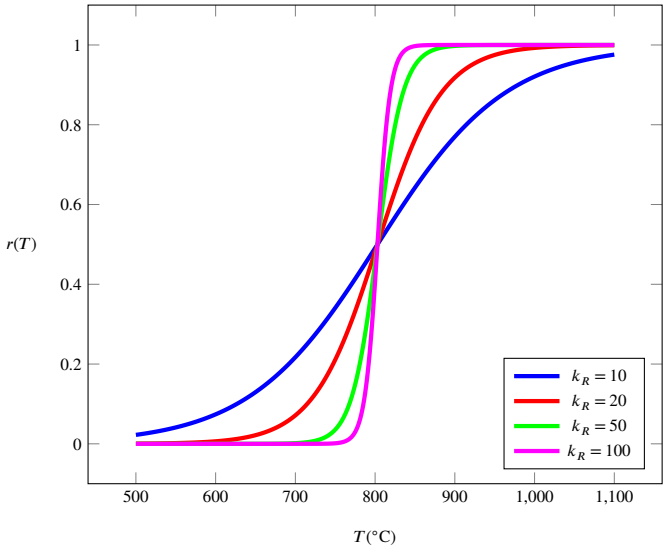

Fig. 7. The effect of parameter k_R on the reset weight function.

$$ {}^{l_i}_{l_j}r_n = \frac{1}{1+\exp\left(\dfrac{-k_R\left({}^{l_i}_{l_j}\mathrm{T}_n - T_R\right)}{T_R}\right)}. \tag{25}$$

Here, ${}^{l_i}_{l_j}r_n$ is the reset weight associated with node n activated during layer l_i when layer l_j is deposited. The reset temperature is given by $T_R = 800\,^{\circ}\mathrm{C}$ [18]. The reset weight function is 1 if ${}^{l_i}_{l_j}\mathrm{T}_n$ is greater than the reset temperature T_R else reset weight is approximately 0. The parameter k_R controls the shape of the reset weight function. The influence of the parameter k_R on the reset weight function is shown in Fig. 7. In this study, $k_R = 100$ is chosen.

For the thermal history shown in Fig. 5 the temperature at time $t = \tau^{\mathfrak{h}}_{l_j} + \Delta\tau^{l_i}_{l_j}$ is shown by the square-shaped markers. The square-shaped markers shown in black and red color indicate the reset weight of 0 and 1, respectively. It can be observed that four process intervals have temperatures above the reset temperature. The last process interval of these is identified by applying an additional sequential weight to each process interval. The sequential weight is given as:

$$ {}^{l_i}_{l_j}s_n = a^{(j-i+1)}, \quad \text{where,} \quad a > 1. \tag{26}$$

Here, ${}^{l_i}_{l_j}s_n$ is the sequential weight assigned to node n during the deposition of the layer l_j. The condition on base $a > 1$ ensures that the weight grows exponentially and the weight of each subsequent process interval is higher than the previous one. Based on the base a, the relative contribution from the last process interval to the aggregated function can be tuned. This can be understood by comparing the last sequential weight to the sum of all sequential weights:

$$ f = \frac{a^{j-i+1}}{\sum_{j=i}^{L} a^{j-i+1}}. \tag{27}$$

Since the sequence in the denominator is a geometric progression, the above equation can be reduced to:

$$ f = \left(1 - \frac{1}{a}\right)\frac{1}{1 - \dfrac{1}{a^{j-i+1}}}. \tag{28}$$

For the condition $j >> i$, the term $1/a^{j-i+1} \to 0$. Thus, the fraction can be approximated as:

$$ f \approx 1 - \frac{1}{a}. \tag{29}$$

Thus, for $a = 2$ and $a = 100$ the contribution from the last process interval tends to 50% and 99%, respectively. Using a higher value of a thus makes the contribution of the last process interval more dominant. However, considering higher a values may lead to numerical overflow during computational implementation as the sequential weight function grows exponentially. Therefore, $a = 2$ is considered in this study, which means that the last process interval will contribute 50% in the cooling time estimation.

The reset and sequential weights are combined together to emphasize the cooling time of the decisive process interval as

$$ \tilde{\mathfrak{t}}_n = \frac{\sum_{j=i}^{L}\left[{}^{l_i}_{l_j}\tilde{\mathfrak{t}}_n\right]\left[{}^{l_i}_{l_j}r_n\right]\left[{}^{l_i}_{l_j}s_n\right]}{\sum_{j=i}^{L}\left[{}^{l_i}_{l_j}r_n\right]\left[{}^{l_i}_{l_j}s_n\right]}. \tag{30}$$

Through this aggregation, the contribution of the cooling time in the critical temperature range for the decisive cycle will be dominant. For the thermal history shown in Fig. 5, the reset and sequential weights corresponding to the first six process intervals are given in Fig. 8. It can be clearly observed that for the first four cycles, the reset weights are equal to 1. For subsequent thermal cycles, the reset weight is approximately 0. Therefore, reset weight successfully identifies the four cycles with temperatures above reset temperature. The combination of reset and sequential weight shows that the weight on the fourth cycle is the highest. Moreover, the contribution from the fourth cycle is 53%. The cooling times in the critical temperature range for each process interval after deposition of the considered node and their contribution to the aggregated cooling time are shown in Fig. 9.

It remains to verify the proposed continuous decisive cooling time identification in the entire domain. For this purpose, the aggregated cooling time field is compared with the actual decisive cooling time field in Fig. 10. It is observed that the proposed aggregation scheme captures the decisive cooling times well. A percentage error between the actual and aggregated time is shown in Fig. 11. The errors encountered are due to the use of continuous and differentiable mathematical functions to formulate a gradient-based optimization problem. The error is low in the region where cooling times are high and vice versa. Moreover, the error is high in the intermediate regions which are dominant at the interface of the solid and void regions.

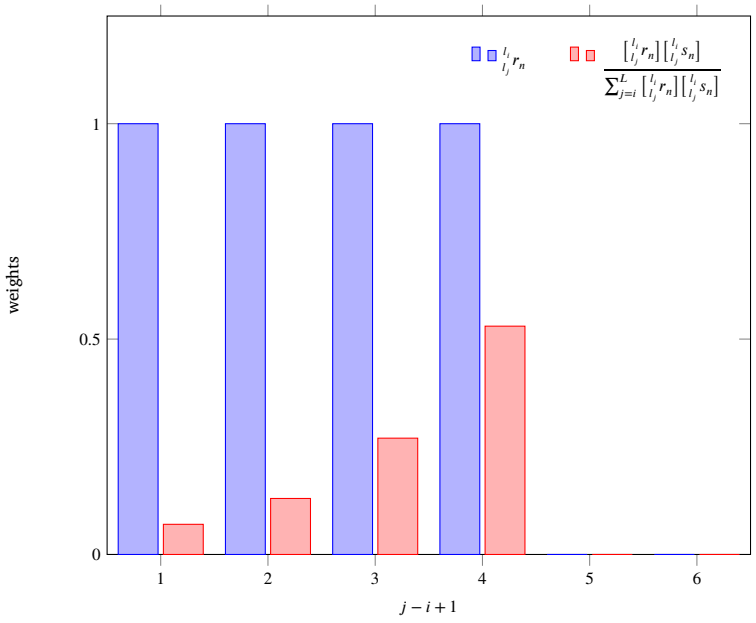

Fig. 8. Reset weights and aggregated weights assigned to the cooling time of the first six process intervals for the thermal history shown in Fig. 5.

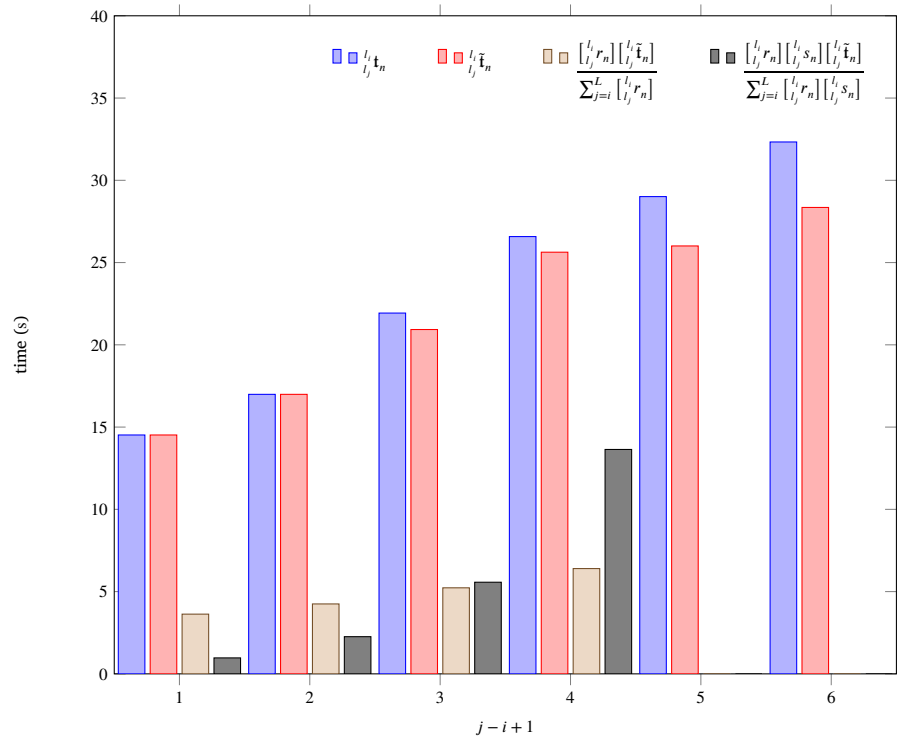

Fig. 9. The total time and the cooling time in the critical temperature range for the first six process intervals of the thermal history shown in Fig. 5. The corresponding contribution to the aggregated weighted cooling time by each process interval is also shown.

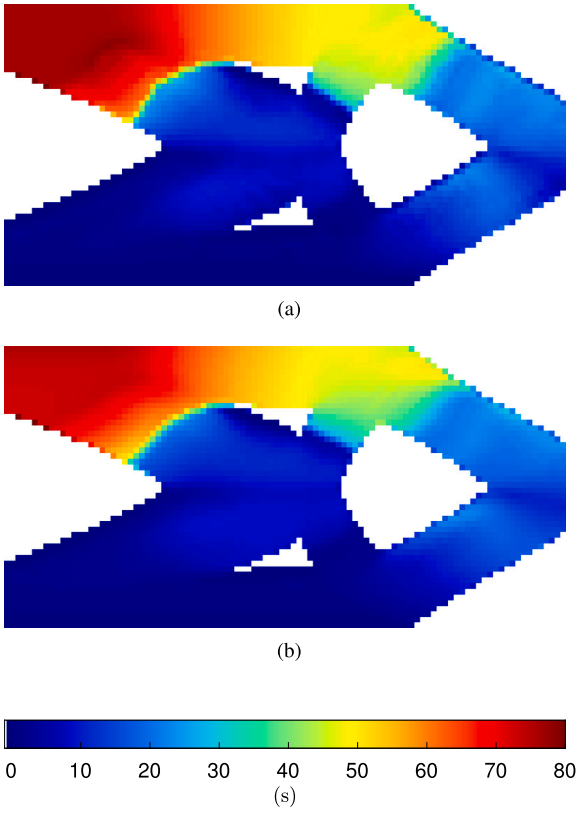

Fig. 10. Comparison between (a) the actual cooling time of the decisive process interval and (b) the aggregated cooling time.

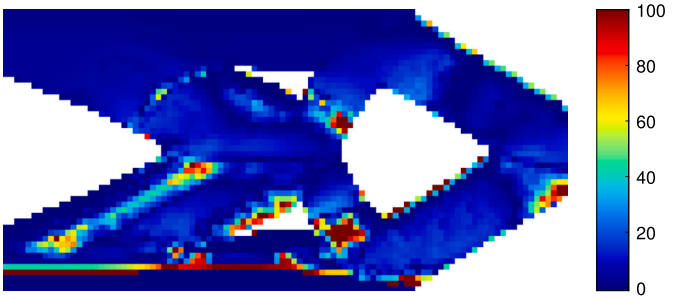

Fig. 11. The percentage error between the actual time and the aggregated time, shown in Fig. 10.

4.3. Optimization problem

In order to control the cooling times of the decisive cooling cycle in the critical temperature range, we define the following optimization problem:

$$\min_{\boldsymbol{\rho}} \quad c = \frac{1}{2}\sum_{\Omega_N} \mathbf{u}_e^{\mathrm{T}}\mathbf{k}_e(\rho_e)\mathbf{u}_e, \tag{31}$$

$$\text{s.t.} \quad \mathbb{K}\mathbf{u} = \mathbf{f}. \tag{32}$$

$$\mathbf{C}_{l_i}(\rho)\dot{\mathbf{T}}_{l_i} + \mathbf{K}_{l_i}(\rho)\mathbf{T}_{l_i} = \mathbf{Q}_{l_i}, \quad \forall l_i \in \Omega_L. \tag{33}$$

$$\mathbf{T}_{l_i} = \mathbf{T}_0, \quad t = t_{l_{i-1}}. \tag{34}$$

$$\underline{\tau} \le \frac{1}{N_c}\sum_{\Omega_c} \tilde{\mathbf{t}}_n \le \bar{\tau}. \tag{35}$$

$$V(\rho) \le V_0. \tag{36}$$

$$0 \le \rho_e \le 1, \quad \forall e \in \Omega_N. \tag{37}$$

In the above problem, the compliance of the structure is minimized considering new constraints regarding the manufacturing process of the design. Eq. (35) is the average cooling time constraint imposed during the manufacturing process in a control volume Ω_c. For simplicity, the average is considered instead of a more nonlinear measure such as a (smooth) maximum. $\bar{\tau}$ and $\underline{\tau}$ are the maximum and minimum allowed values of the average time spent by the number of nodes (N_c) in the control volume in the critical temperature range. A gradient-based optimization approach is used for which calculation of the design sensitivities of objectives and constraints is important. The design sensitivities of the compliance objective and volume constraint are well known [25]. The design sensitivity of the cooling time constraint with respect to the design variable is given in Appendix A.

The considered loadcase for which the compliance is minimized is shown in Fig. 12. Two control volumes and non-design domains, Ω_{c_1} and Ω_{c_2}, are considered in the examples in the next section. Average cooling times are controlled in these control volumes for selected values of $\bar{\tau}$ and $\underline{\tau}$. To demonstrate the degree of control of thermal history and associated microstructure development, initially, the cooling times are constrained in each control volume individually and thereafter, simultaneously. A complete flowchart of the optimization framework is given in Fig. 13.

The constrained cooling time values $\underline{\tau}$ and $\bar{\tau}$ are chosen by considering the standard compliance minimized design Fig. 2 as a reference design. For this reference design, the average normalized weighted cooling times in control volume Ω_{c_1} and Ω_{c_2} are approximately 80 s and 6 s, respectively. The locations of the control volume are selected such that material is only deposited below Ω_{c_1}. In contrast, the material is deposited both above and below control volume Ω_{c_2}. Thus, for Ω_{c_1}, the heat input has to be facilitated by the design changes below the control volume, while for Ω_{c_2} design changes are expected above and below the control volume.

5. Results and discussions

As mentioned earlier, first the effect of the time step on the solution of the transient heat conduction equation is examined. Subsequently, the designs obtained by solving the topology optimization problem constraining cooling time in a single control volume and both control volumes simultaneously are presented in this section. Furthermore salient points of the methodology will be discussed along with the results.

5.1. Effect of time steps

The effect of time step Δt on the thermal history of a node of the compliance minimized design is shown in Fig. 14. It can be observed that the time step has a distinct effect on the thermal history calculation. By reducing the time step the solution converges to the actual solution of the transient thermal heat conduction problem considered in this study. It is observed that the Forward Euler Scheme (explicit) is not stable when $\Delta t > 0.005$ s. Therefore, the Backward Euler scheme (implicit) is chosen due to its unconditional stability. However, increasing the time step while using an implicit scheme introduces numerical errors in the solution compared to the converged solution as depicted in Fig. 14.

The wall clock times to complete the process simulation with MATLAB through Implicit and Explicit schemes with various time steps are given in Table 2. The wall clock time to obtain the converged solution is 7.5 hr (28120 s). The same amount of time is also required for the design sensitivities calculation. The number of equations required to calculate design sensitivities, see Section Appendix A, is the same as of the transient heat transfer problem solved in the process simulation. TO with the converged thermal process simulation solution for a modest 100 iterations takes about two months. This extravagant time required for optimization bounds us to use coarser time steps to get initial results. For instance, by using a time step $\Delta t = 0.1$ to 1.0 s the optimized designs

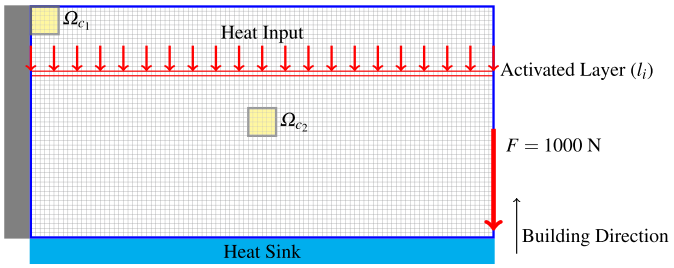

Fig. 12. Schematic illustration of the cantilever beam problem with Consideration of WAAM Process induced material properties. The rectangular domain with blue borders is the design domain, discretized with a structured mesh of bilinear quadrilateral elements. The left boundary of the domain is rigidly fixed and a point load is applied indicated with a thick red arrow. The deposition is considered in a layer-by-layer manner. The heat input is applied to the deposited layer as indicated by thin red arrows. The translucent yellow regions are the control volumes that remain solid. The decisive cooling times are constrained in these control volumes.

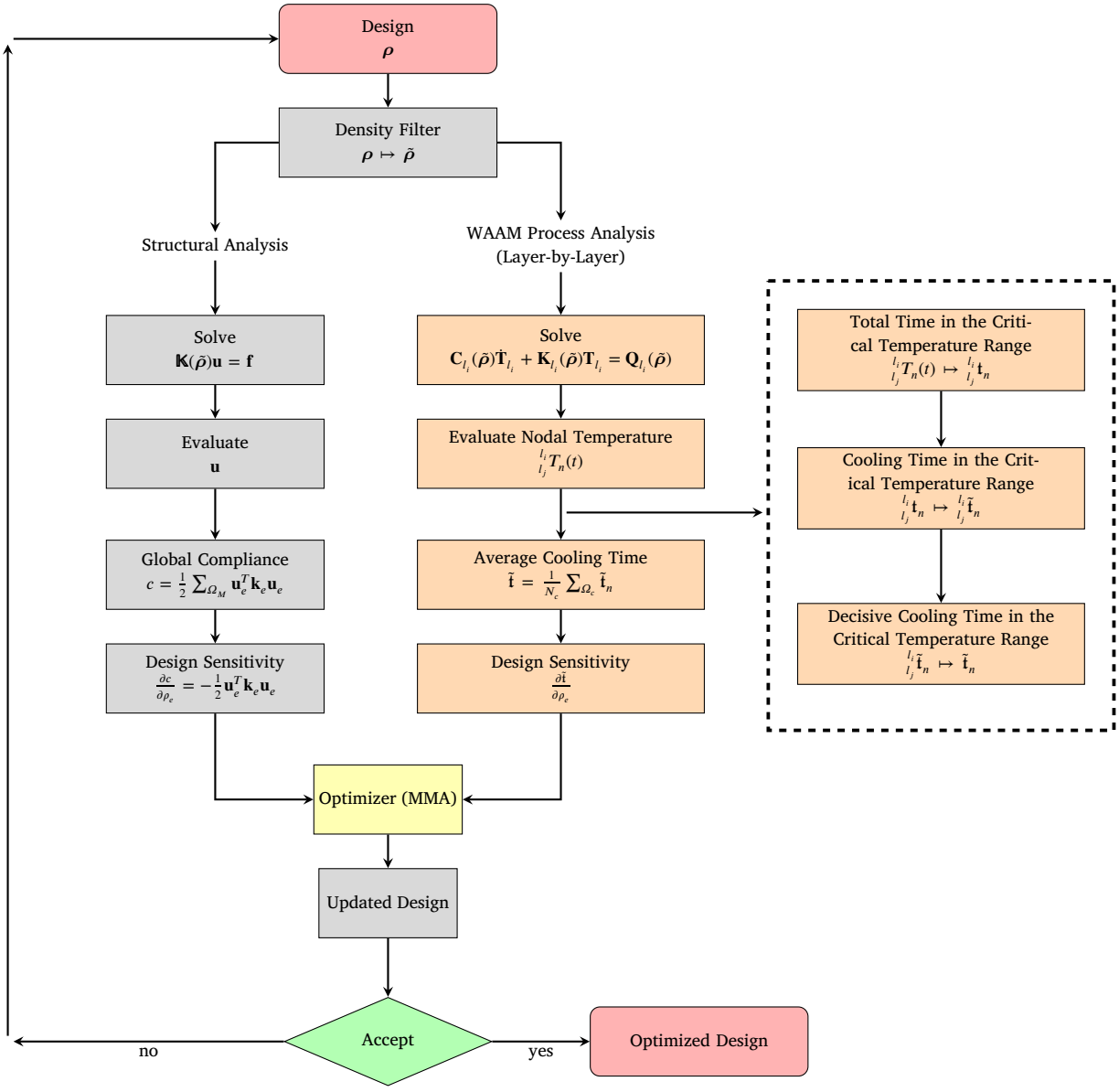

Fig. 13. Flow chart of the novel design optimization framework for minimum compliance while constraining the average cooling time in the design domain to control the microstructure development during the WAAM process.

Table 2
The effect of time step on the total wall clock time to perform the simplified thermal process model. The number of DOFs = 5252, the total time per layer = 200 s, and the Number of layers = 50.

Time Integration Scheme	Implicit	Implicit	Implicit	Implicit	Explicit
Time step	1 s	0.1 s	0.01 s	0.005 s	0.005 s
Number of time steps per layer	200	2000	20000	40000	40000
Total wall clock time for process simulation	240 s	1489 s	14100 s	28120 s	28120 s

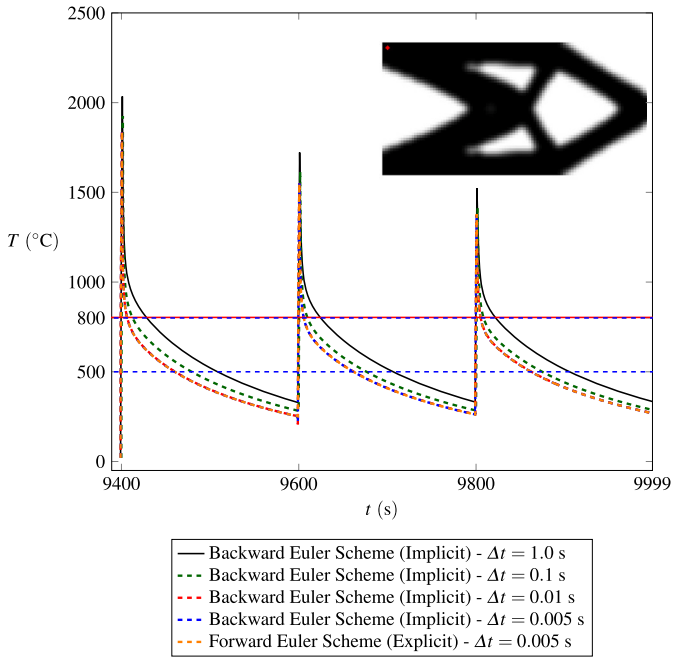

Fig. 14. Effect of the time step on the thermal history of the indicated node of the compliance minimized design shown as an inset.

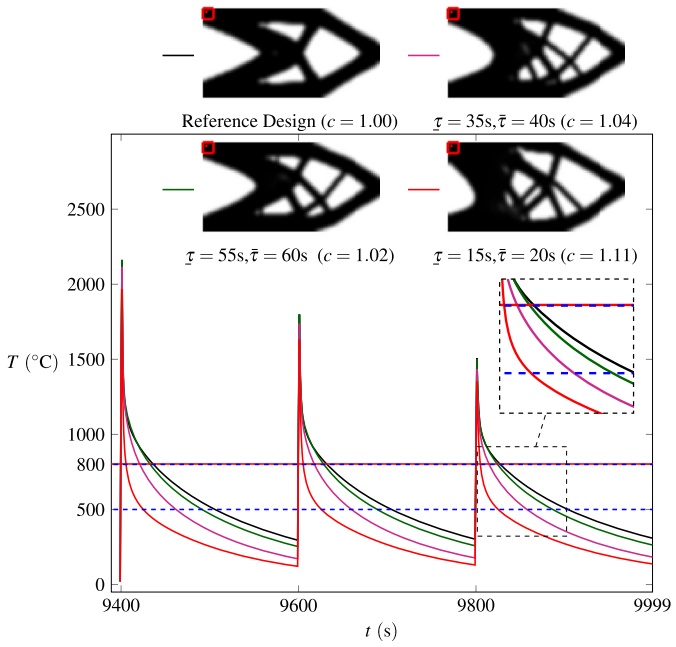

Fig. 15. The optimized design obtained by controlling the average cooling rate of the control volume Ω_{c_1} and transient thermal history of the node represented by red obtained by process simulation for selected values of $\underline{\tau}$ and $\bar{\tau}$.

can be obtained in the duration of several weeks to several days. Here we make the pragmatic choice to use $\Delta t = 1.0$ s for our optimization study to obtain results in a few days.

5.2. Optimized designs

Optimized designs with constraints on the average cooling time only in single control volume Ω_{c_1} and Ω_{c_2} are given in Fig. 15 and Fig. 16, respectively. The results in Fig. 15 show that in order to reduce the decisive cooling time in the critical temperature range the optimizer shortens and broadens the path of heat transfer to the heat sink below Ω_{c_1}. The heat transfer is facilitated in a controlled manner and the transient thermal history shows that the decisive cooling time has clearly reduced. The results in Fig. 16 show that the decisive cooling time is increased by modifying the design above and below the control volume. The optimizer disintegrates the thick straight bar connected to the control volume into thin features to reduce the incoming heat to the control volume during AM. Moreover, the material beneath the control volume is eroded to hinder the heat transfer to the heat sink.

The cooling time of the decisive cycle of the optimized designs, corresponding predicted yield strength, and Vickers Hardness are shown in Fig. 17 and Fig. 18 for control volume Ω_{c_1} and Ω_{c_2}, respectively. The result shows that the cooling time and hence the local hardness and yield strength can be increased or decreased through design modifications.

The optimized designs with constraints on the average cooling times on both control volumes simultaneously are shown in Fig. 19. For the optimized cases shown in Fig. 19 similar observations can be made as in the previous instances in which only one control volume is controlled. The results in Fig. 19 show that the cooling time, yields strength, and

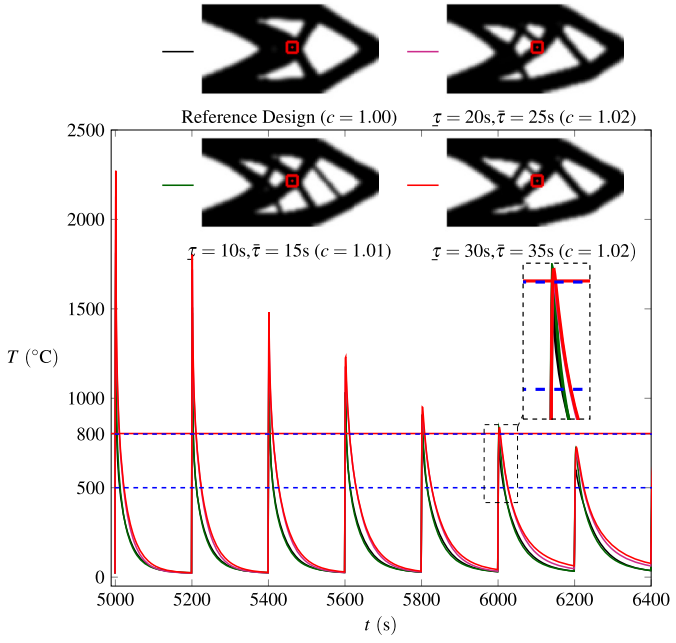

Fig. 16. Optimized design obtained by controlling the average cooling rate of the control volume Ω_{c_2} and Transient thermal history of the same node represented by red dot obtained by process simulation.

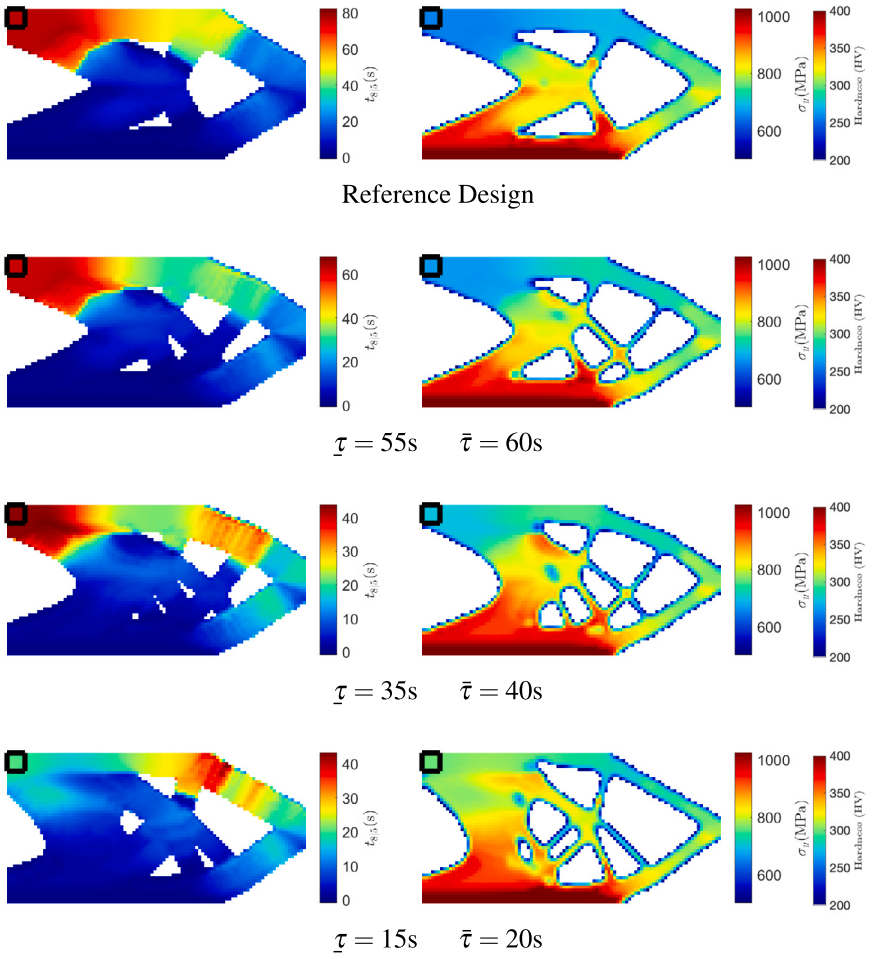

Fig. 17. The left column represents cooling time (in s) of the decisive cooling cycle experienced by the optimized design with a constraint average cooling time in the control volume Ω_{C_1}. The right column is the corresponding predicted Yield Strength and Vickers Hardness estimated by Eq. (17) and Eq. (16), respectively.

Vickers hardness of different locations in the design domain can be influenced simultaneously.

The compliance of all the optimized designs with average cooling rate constraints has increased compared to the reference design. The increase in compliance is due to the local design changes to fulfill the average cooling time constraint in the local design domain. The increase in compliance ranges from $1-11\%$ which is insignificant due to the local design modifications in the design to satisfy the average cooling rate constraint.

6. Conclusions and future work

In this work, a novel TO framework is developed to control an important aspect of metal microstructure, which is solid-state phase fractions by controlling cooling times during the AM process. For AM, the cooling time of a decisive cooling cycle in a critical temperature range is essential. The cooling times directly impact the microstructure and resultant mechanical properties. A novel methodology is presented to isolate the cooling time in the critical temperature range of the decisive cooling cycle from the multiple heating and cooling cycles experienced by the AM parts. The presented method is differentiable and is hence suitable for use in gradient-based topology optimization. The cooling times are constrained at desired design locations during optimization. The results show that the cooling times of the decisive cooling cycle can be increased and reduced to adjust the yield strength in a control volume by facilitating and hindering the incoming and outgoing heat flow toward the heat sink through design optimization.

In this study, the complete transient history of the AM process is evaluated and used for optimization purposes. The computational cost to evaluate the complete transient thermal history and design sensitivities of the cooling time is 960 times higher than the reference TO problem without AM process constraints in the 2D examples investigated. The computational cost increases with the increase in the spatial resolution of the design, the number of layers required to produce the part through AM process, the number of degrees of freedom constrained during optimization, and the temporal resolution of the time integration scheme.

There are multiple research directions based on the conclusions. The computation cost involves in optimization is immense and there is a need to devise a strategy to lower the computational costs. The computation cost can be reduced by parallel computation of the transient thermal history of each layer which is currently performed sequentially in this study. Consequently, the computation cost of the total process simulation will be factored by the total number of layers in the process. For example, in our case, the wall clock time for the total process simulation of 50 layers is 240 s, see Table 2. Through parallel computing, the total wall clock time to evaluate the complete transient thermal history can be reduced to 4.8 s. This enables the transient thermal history to be obtained quickly. Another method to accelerate the process is using an adaptive time-stepping approach. In this approach, the time steps can be reduced in the region of interest and increased elsewhere. For instance, the time stepping in the critical temperature range could be refined, otherwise, it could be coarse. This will enable a reduction of the number of times the system of equations is to be solved in regions other than the critical temperature range. It will pose a requirement to

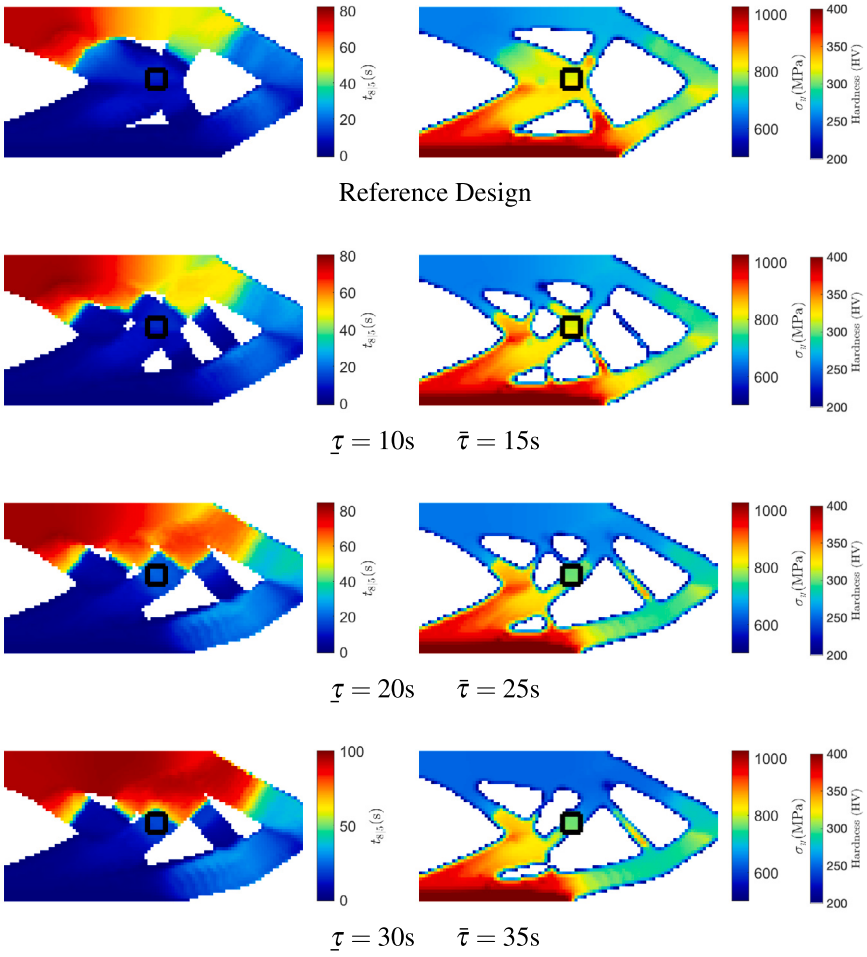

Fig. 18. The left column represents the cooling time (in s) of the decisive cooling cycle experienced by the optimized design with a constraint average cooling time in the control volume Ω_{C_2}. The right column is the corresponding predicted Yield Strength and Vickers Hardness estimated by Eq. (17) and Eq. (16), respectively.

store an array of time steps used in the study which would be used for the design sensitivity calculation. Reducing the computational cost will also allow the extension of this approach to 3D. Once these results get realized in 3D, the design can be manufactured by AM, and validation of the results can be achieved. The validation of the optimized results can be done by comparing the hardness maps of the optimized design with the hardness maps of the part manufactured by WAAM.

Another direction of research is on the mechanics side of the problem. As shown in this work, the yield strength is process-dependent and varies locally in the design based on the thermal history. A new stress constraint can be imposed in which the actual stress is evaluated from the loading and boundary conditions, and the local yield strength is estimated from the process simulation. Through this stress constraint efficient designing of the mechanical properties in the entire design domain can be achieved.

Moreover, as discussed in the introduction, in this study effect of tempering is neglected which also has an effect on the mechanical properties. The tempering depends on the amount of time the material experiences in the critical temperature range which is lower than the critical temperature range of solid-state phase transformation for HSLA steels. The window functions used in this study can be used to include the effect of tempering. To extend the methodology to titanium alloys, it is required to know thermal material properties, the temperature above which the room temperature solid-state phases transform to the high-temperature phase, and the critical temperature range in which the cooling rate influences the phase transformation. Extending the method to other alloys with solid-state phase transformation dissimilar to HSLA, the material-specific microstructural response of the alloy of interest to thermal evolution during AM should be developed. Furthermore, the grain or cell size of a wide range of alloys can be controlled by controlling the solidification rates in a different critical temperature range. However, this would require estimating very high cooling rates from the thermal simulations, which would considerably increase the computational time.

Finally, although this work has focused on design changes under the assumption that the AM process cannot be influenced, the proposed approach also applies to problems where the part design is fixed and the process parameters can be optimized. The presented sensitivity analysis remains largely the same, apart from the fact that the heat load becomes dependent on the optimization variables instead of the thermal properties. This variant also presents an interesting direction for future research.

Declaration of competing interest

The authors declare the following financial interests/personal relationships which may be considered as potential competing interests:

Vibhas Mishra reports financial support was provided by M2i Materials innovation institute. Vibhas Mishra reports financial support was provided by Dutch Research Council (grant No. P16-46).

Data availability

Data will be made available on request.

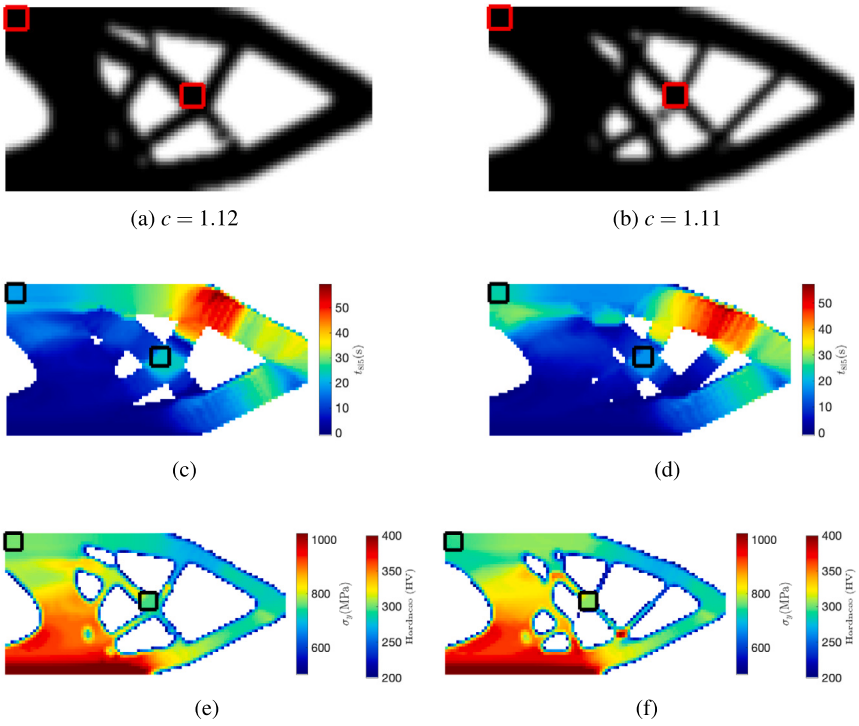

Fig. 19. Optimized design obtained by controlling the average cooling time of the control volumes Ω_{c_1} and Ω_{c_2} simultaneously. (a) For Ω_{c_1} : $\underline{\tau} = 15$ s, $\bar{\tau} = 20$ s, for Ω_{c_2} : $\underline{\tau} = 20$ s, $\bar{\tau} = 25$ s (b) For Ω_{c_1} : $\underline{\tau} = 20$ s, $\bar{\tau} = 25$ s, for Ω_{c_2} : $\underline{\tau} = 15$ s, $\bar{\tau} = 20$ s. (c) and (d) are the corresponding cooling time for both the optimized designs, respectively. (e) and (f) are the corresponding Yield Strength and Vickers Hardness values obtained by Eq. (17) and Eq. (16), respectively.

Acknowledgements

This research was carried out under project number S17024a in the framework of the Partnership Program of the Materials innovation institute M2i (www.m2i.nl) and the Technology Foundation TTW (www.stw.nl), which is part of the Netherlands Organisation for Scientific Research (www.nwo.nl). We also thank Prof. Krister Svanberg from KTH in Stockholm, Sweden for providing the MATLAB implementation of MMA algorithm.

Appendix A. Sensitivity calculations

The design sensitivity calculation of the average cooling time constraint given in Eq. (35) is as follows:

$$\frac{\partial}{\partial \rho_e}\left[\frac{1}{N_c}\sum_{\Omega_c}\tilde{\mathbf{t}}_n\right] = \frac{1}{N_c}\sum_{\Omega_c}\frac{\partial \tilde{\mathbf{t}}_n}{\partial \rho_e} = \frac{1}{N_c}\sum_{\Omega_c}\frac{\partial}{\partial \rho_e}\left(\frac{\sum_{j=i}^{L}\left[{}^{l_i}_{l_j}r_n\right]\left[{}^{l_i}_{l_j}s_n\right]\left[{}^{l_i}_{l_j}\tilde{\mathbf{t}}_n\right]}{\sum_{j=i}^{L}\left[{}^{l_i}_{l_j}r_n\right]\left[{}^{l_i}_{l_j}s_n\right]}\right). \tag{A.1}$$

Applying the quotient rule and subsequently, the product rule of derivatives on the above equation will yield

$$\begin{aligned}\frac{\partial \tilde{\mathbf{t}}_n}{\partial \rho_e} = &\frac{1}{\left(\sum_{j=i}^{L}\left[{}^{l_i}_{l_j}r_n\right]\left[{}^{l_i}_{l_j}s_n\right]\right)^2}\left[\left(\sum_{j=i}^{L}\left[{}^{l_i}_{l_j}r_n\right]\left[{}^{l_i}_{l_j}s_n\right]\right)\left(\sum_{j=i}^{L}\frac{\partial\left[{}^{l_i}_{l_j}r_n\right]}{\partial \rho_e}\left[{}^{l_i}_{l_j}r_n\right]\left[{}^{l_i}_{l_j}\tilde{\mathbf{t}}_n\right]\right.\right.\\ &\left.+\sum_{j=i}^{L}\left[{}^{l_i}_{l_j}r_n\right]\left[{}^{l_i}_{l_j}s_n\right]\frac{\partial\left[{}^{l_i}_{l_j}\tilde{\mathbf{t}}_n\right]}{\partial \rho_e}\right)\\ &\left.-\left(\sum_{j=i}^{L}\left[{}^{l_i}_{l_j}r_n\right]\left[{}^{l_i}_{l_j}s_n\right]\left[{}^{l_i}_{l_j}\tilde{\mathbf{t}}_n\right]\right)\left(\sum_{j=i}^{L}\left[{}^{l_i}_{l_j}s_n\right]\frac{\partial\left[{}^{l_i}_{l_j}r_n\right]}{\partial \rho_e}\right)\right].\end{aligned} \tag{A.2}$$

In above equation, $\frac{\partial\left[{}^{l_i}_{l_j}\tilde{\mathbf{t}}_n\right]}{\partial \rho_e}$ and $\frac{\partial\left[{}^{l_i}_{l_j}r_n\right]}{\partial \rho_e}$ are important terms which need to be evaluated. The sequential weight is independent of the design variable, thus, the design sensitivity of the sequential weight is 0. The calculation of $\frac{\partial\left[{}^{l_i}_{l_j}\tilde{\mathbf{t}}_n\right]}{\partial \rho_e}$ is done using Eq. (24). In subsequent equations, the dependent variable parentheses are dropped to show the calculation in a succinct manner. Applying the product rule and chain rule gives

$$\frac{\partial\left[{}^{l_i}_{l_j}\tilde{\mathbf{t}}_n\right]}{\partial \rho_e} = \int_{\tau_{l_{j-1}}}^{\tau_{l_j}}\left[{}^{l_i}_{l_j}H_n\right]\left(\bar{H}\frac{\partial \underline{H}}{\partial\left[{}^{l_i}_{l_j}T_n\right]} + \frac{\partial \bar{H}}{\partial\left[{}^{l_i}_{l_j}T_n\right]}\underline{H}\right)\frac{\partial\left[{}^{l_i}_{l_j}T_n\right]}{\partial \rho_e}dt. \tag{A.3}$$

Eq. (19) and Eq. (20) are used to evaluate $\frac{\partial \underline{H}}{\partial\left[{}^{l_i}_{l_j}T_n\right]}$ and $\frac{\partial \bar{H}}{\partial\left[{}^{l_i}_{l_j}T_n\right]}$. The derivative operations are trivial, therefore, not presented here. However, the evaluation of the term $\frac{\partial\left[{}^{l_i}_{l_j}T_n\right]}{\partial \rho_e}$ is not trivial. Adjoint method is employed to calculate $\frac{\partial\left[{}^{l_i}_{l_j}T_n\right]}{\partial \rho_e}$. For this purpose, let us introduce following representation for the nodal temperature

$$\left[{}^{l_i}_{l_j}T_n\right](t) := \mathbf{R}_n^T\mathbf{T}_{l_j}(t). \tag{A.4}$$

Here, $\mathbf{R}_n$ is the array of length equal to $\mathbf{T}_{l_j}$. The array $\mathbf{R}_n$ has entry 1 at the interested degree of freedom, i.e. node n, and 0 elsewhere. Therefore, the Eq. (A.3) becomes

$$\frac{\partial\left[{}^{l_i}_{l_j}\tilde{\mathbf{t}}_n\right]}{\partial \rho_e} = \int_{\tau_{l_{j-1}}}^{\tau_{l_j}}\left[{}^{l_i}_{l_j}H_n\right]\left(\bar{H}\frac{\partial \underline{H}}{\partial\left[{}^{l_i}_{l_j}T_n\right]} + \frac{\partial \bar{H}}{\partial\left[{}^{l_i}_{l_j}T_n\right]}\underline{H}\right)\mathbf{R}_n^T\frac{\partial \mathbf{T}_{l_j}}{\partial \rho_e}dt. \tag{A.5}$$

Note, $\left[{}^{l_i}_{l_j}H_n\right]=0$, if $\tau_{l_{j-1}} \le t < \tau^{\mathfrak{h}}_{l_j} + \Delta\tau^{l_i}_{l_j}$, therefore the contribution to the sensitivities of the above integration in range $\tau_{l_{j-1}} \le t < \tau^{\mathfrak{h}}_{l_j} + \Delta\tau^{l_i}_{l_j}$ will be 0.

Similar to $\frac{\partial\left[{}^{l_i}_{l_j}\tilde{\mathbf{t}}_n\right]}{\partial\rho_e}$, $\frac{\partial\left[{}^{l_i}_{l_j}r_n\right]}{\partial\rho_e}$ can also be represented in the integral form which includes $\frac{\partial\mathbf{T}_{l_j}}{\partial\rho_e}$ term. To evaluate the design sensitivities of the weight term Eq. (25) is used. Applying chain rule we get

$$\frac{\partial\left[{}^{l_i}_{l_j}r_n\right]}{\partial\rho_e}=\frac{\partial\left[{}^{l_i}_{l_j}r_n\right]}{\partial\left[{}^{l_i}_{l_j}\mathrm{T}_n\right]}\frac{\partial\left[{}^{l_i}_{l_j}\mathrm{T}_n\right]}{\partial\rho_e}. \tag{A.6}$$

The term $\frac{\partial\left[{}^{l_i}_{l_j}r_n\right]}{\partial\left[{}^{l_i}_{l_j}\mathrm{T}_n\right]}$ is trivial to calculate. To calculate the non-trivial term $\frac{\partial\left[{}^{l_i}_{l_j}\mathrm{T}_n\right]}{\partial\rho_e}$ we re-write the $\left[{}^{l_i}_{l_j}\mathrm{T}_n\right]$ as follows:

$$\left[{}^{l_i}_{l_j}\mathrm{T}_n\right]=\int_{-\infty}^{\infty}\delta(t-(\tau^{\mathfrak{h}}_{l_j}+\Delta\tau^{l_i}_{l_j}))\mathbf{R}_n^T\mathbf{T}_{l_j}(t)dt. \tag{A.7}$$

Now, taking the design sensitivity of the above equation we get:

$$\frac{\partial\left[{}^{l_i}_{l_j}\mathrm{T}_n\right]}{\partial\rho_e}=\int_{-\infty}^{\infty}\delta(t-(\tau^{\mathfrak{h}}_{l_j}+\Delta\tau^{l_i}_{l_j}))\mathbf{R}_n^T\frac{\partial\mathbf{T}_{l_j}}{\partial\rho_e}dt=\int_{\tau_{l_{j-1}}}^{\tau_{l_j}}\delta(t-(t^{\mathfrak{h}}_{l_j}+\Delta\tau^{l_i}_{l_j}))\mathbf{R}_n^T\frac{\partial\mathbf{T}_{l_j}}{\partial\rho_e}dt. \tag{A.8}$$

Where, δ is the dirac delta function which is equal to 1 at $t=\tau^{\mathfrak{h}}_{l_j}+\Delta\tau^{l_i}_{l_j}$.

Both the term $\frac{\partial\left[{}^{l_i}_{l_j}\tilde{\mathbf{t}}_n\right]}{\partial\rho_e}$ and $\frac{\partial\left[{}^{l_i}_{l_j}r_n\right]}{\partial\rho_e}$ represented in the form of $\frac{\partial\mathbf{T}_{l_j}}{\partial\rho_e}$ can be substituted in Eq. (A.2). Firstly, we rewrite the terms in Eq. (A.2) by grouping the terms associated to $\frac{\partial\left[{}^{l_i}_{l_j}\tilde{\mathbf{t}}_n\right]}{\partial\rho_e}$ and $\frac{\partial\left[{}^{l_i}_{l_j}r_n\right]}{\partial\rho_e}$ together as follows:

$$\begin{aligned}\frac{\partial\tilde{\mathbf{t}}_n}{\partial\rho_e}=\frac{1}{\left(\sum_{j=i}^{L}\left[{}^{l_i}_{l_j}r_n\right]\left[{}^{l_i}_{l_j}s_n\right]\right)^2}\sum_{j=i}^{L}\Bigg[&\Bigg\{\Bigg(\sum_{j=i}^{L}\left[{}^{l_i}_{l_j}r_n\right]\left[{}^{l_i}_{l_j}s_n\right]\Bigg)\left[{}^{l_i}_{l_j}r_n\right]\left[{}^{l_i}_{l_j}\tilde{\mathbf{t}}_n\right]\\&-\Bigg(\sum_{j=i}^{L}\left[{}^{l_i}_{l_j}r_n\right]\left[{}^{l_i}_{l_j}s_n\right]\left[{}^{l_i}_{l_j}\tilde{\mathbf{t}}_n\right]\Bigg)\left[{}^{l_i}_{l_j}s_n\right]\Bigg\}\frac{\partial\left[{}^{l_i}_{l_j}r_n\right]}{\partial\rho_e}\\&+\Bigg\{\Bigg(\sum_{j=i}^{L}\left[{}^{l_i}_{l_j}r_n\right]\left[{}^{l_i}_{l_j}s_n\right]\Bigg)\left[{}^{l_i}_{l_j}r_n\right]\left[{}^{l_i}_{l_j}s_n\right]\Bigg\}\frac{\partial\left[{}^{l_i}_{l_j}\tilde{\mathbf{t}}_n\right]}{\partial\rho_e}\Bigg].\end{aligned} \tag{A.9}$$

Now, substituting the design sensitivities $\frac{\partial\left[{}^{l_i}_{l_j}\tilde{\mathbf{t}}_n\right]}{\partial\rho_e}$ and $\frac{\partial\left[{}^{l_i}_{l_j}r_n\right]}{\partial\rho_e}$ from Eq. (A.5), Eq. (A.6) and Eq. (A.8) in above equation we get:

$$\begin{aligned}\frac{\partial\tilde{\mathbf{t}}_n}{\partial\rho_e}=\frac{1}{\left(\sum_{j=i}^{L}\left[{}^{l_i}_{l_j}r_n\right]\left[{}^{l_i}_{l_j}s_n\right]\right)^2}\sum_{j=i}^{L}\Bigg[&\Bigg\{\Bigg(\sum_{j=i}^{L}\left[{}^{l_i}_{l_j}r_n\right]\left[{}^{l_i}_{l_j}s_n\right]\Bigg)\left[{}^{l_i}_{l_j}r_n\right]\left[{}^{l_i}_{l_j}\tilde{\mathbf{t}}_n\right]\\&-\Bigg(\sum_{j=i}^{L}\left[{}^{l_i}_{l_j}r_n\right]\left[{}^{l_i}_{l_j}s_n\right]\left[{}^{l_i}_{l_j}\tilde{\mathbf{t}}_n\right]\Bigg)\left[{}^{l_i}_{l_j}s_n\right]\Bigg\}\frac{\partial\left[{}^{l_i}_{l_j}r_n\right]}{\partial\left[{}^{l_i}_{l_j}\mathrm{T}_n\right]}\\&\int_{\tau_{l_{j-1}}}^{\tau_{l_j}}\delta(t-(t^{\mathfrak{h}}_{l_j}+\Delta\tau^{l_i}_{l_j}))\mathbf{R}_n^T\frac{\partial\mathbf{T}_{l_j}}{\partial\rho_e}dt\\&+\Bigg\{\Bigg(\sum_{j=i}^{L}\left[{}^{l_i}_{l_j}r_n\right]\left[{}^{l_i}_{l_j}s_n\right]\Bigg)\left[{}^{l_i}_{l_j}r_n\right]\left[{}^{l_i}_{l_j}s_n\right]\Bigg\}\\&\int_{\tau_{l_{j-1}}}^{\tau_{l_j}}\left[{}^{l_i}_{l_j}H_n\right]\left(\bar{H}\frac{\partial\underline{H}}{\partial\left[{}^{l_i}_{l_j}T_n\right]}+\frac{\partial\bar{H}}{\partial\left[{}^{l_i}_{l_j}T_n\right]}\underline{H}\right)\mathbf{R}_n^T\frac{\partial\mathbf{T}_{l_j}}{\partial\rho_e}dt\Bigg].\end{aligned} \tag{A.10}$$

The above equation can be rewritten as follows:

$$\begin{aligned}\frac{\partial\tilde{\mathbf{t}}_n}{\partial\rho_e}=\frac{1}{\left(\sum_{j=i}^{L}\left[{}^{l_i}_{l_j}r_n\right]\left[{}^{l_i}_{l_j}s_n\right]\right)^2}\sum_{j=i}^{L}\Bigg[\int_{\tau_{l_{j-1}}}^{\tau_{l_j}}&\Bigg[\Bigg\{\Bigg(\sum_{j=i}^{L}\left[{}^{l_i}_{l_j}r_n\right]\left[{}^{l_i}_{l_j}s_n\right]\Bigg)\left[{}^{l_i}_{l_j}r_n\right]\left[{}^{l_i}_{l_j}\tilde{\mathbf{t}}_n\right]\\&-\Bigg(\sum_{j=i}^{L}\left[{}^{l_i}_{l_j}r_n\right]\left[{}^{l_i}_{l_j}s_n\right]\left[{}^{l_i}_{l_j}\tilde{\mathbf{t}}_n\right]\Bigg)\left[{}^{l_i}_{l_j}s_n\right]\Bigg\}\Bigg\{\frac{\partial\left[{}^{l_i}_{l_j}r_n\right]}{\partial\left[{}^{l_i}_{l_j}\mathrm{T}_n\right]}\Bigg\}\Bigg\{\delta(t-(t^{\mathfrak{h}}_{l_j}+\Delta\tau^{l_i}_{l_j}))\Bigg\}\\&+\Bigg\{\Bigg(\sum_{j=i}^{L}\left[{}^{l_i}_{l_j}r_n\right]\left[{}^{l_i}_{l_j}s_n\right]\Bigg)\left[{}^{l_i}_{l_j}r_n\right]\left[{}^{l_i}_{l_j}s_n\right]\Bigg\}\Bigg\{\left[{}^{l_i}_{l_j}H_n\right]\Bigg(\bar{H}\frac{\partial\underline{H}}{\partial\left[{}^{l_i}_{l_j}T_n\right]}\\&+\frac{\partial\bar{H}}{\partial\left[{}^{l_i}_{l_j}T_n\right]}\underline{H}\Bigg)\Bigg\}\Bigg]\mathbf{R}_n^T\frac{\partial\mathbf{T}_{l_j}}{\partial\rho_e}dt\Bigg].\end{aligned} \tag{A.11}$$

The above equation can be condensed to following form:

$$\frac{\partial\tilde{\mathbf{t}}_n}{\partial\rho_e}=\sum_{j\ge i}\int_{\tau_{l_{j-1}}}^{\tau_{l_j}}{}^{l_i}_{l_j}\mathfrak{B}_n\mathbf{R}_n^T\frac{\partial\mathbf{T}_{l_j}}{\partial\rho_e}dt. \tag{A.12}$$

where, ${}^{l_i}_{l_j}\mathfrak{B}_n$ is given as follows:

$$\begin{aligned}{}^{l_i}_{l_j}\mathfrak{B}_n=\frac{1}{\left(\sum_{j=i}^{L}\left[{}^{l_i}_{l_j}r_n\right]\left[{}^{l_i}_{l_j}s_n\right]\right)^2}\Bigg[&\Bigg\{\Bigg(\sum_{j=i}^{L}\left[{}^{l_i}_{l_j}r_n\right]\left[{}^{l_i}_{l_j}s_n\right]\Bigg)\left[{}^{l_i}_{l_j}r_n\right]\left[{}^{l_i}_{l_j}\tilde{\mathbf{t}}_n\right]\\&-\Bigg(\sum_{j=i}^{L}\left[{}^{l_i}_{l_j}r_n\right]\left[{}^{l_i}_{l_j}s_n\right]\left[{}^{l_i}_{l_j}\tilde{\mathbf{t}}_n\right]\Bigg)\left[{}^{l_i}_{l_j}s_n\right]\Bigg\}\Bigg\{\frac{\partial\left[{}^{l_i}_{l_j}r_n\right]}{\partial\left[{}^{l_i}_{l_j}\mathrm{T}_n\right]}\Bigg\}\Bigg\{\delta(t-(t^{\mathfrak{h}}_{l_j}+\Delta\tau^{l_i}_{l_j}))\Bigg\}\\&+\Bigg\{\Bigg(\sum_{j=i}^{L}\left[{}^{l_i}_{l_j}r_n\right]\left[{}^{l_i}_{l_j}s_n\right]\Bigg)\left[{}^{l_i}_{l_j}r_n\right]\left[{}^{l_i}_{l_j}s_n\right]\Bigg\}\Bigg\{\left[{}^{l_i}_{l_j}H_n\right]\Bigg(\bar{H}\frac{\partial\underline{H}}{\partial\left[{}^{l_i}_{l_j}T_n\right]}\\&+\frac{\partial\bar{H}}{\partial\left[{}^{l_i}_{l_j}T_n\right]}\underline{H}\Bigg)\Bigg\}\Bigg].\end{aligned} \tag{A.13}$$

To calculate the total sensitivities, the sensitivities of the state equation with the Lagrange multiplier $\boldsymbol{\lambda}_{l_j}(t)$ given as follows can be added to Eq. (A.12).

$$\boldsymbol{\lambda}_{l_j}^T\frac{\partial}{\partial\rho_e}(\mathbf{C}_{l_j}\dot{\mathbf{T}}_{l_j}+\mathbf{K}_{l_j}\mathbf{T}_{l_j}-\mathbf{Q}_{l_j})=\mathbf{0}. \tag{A.14}$$

Eq. (A.12) becomes

$$\frac{\partial\tilde{\mathbf{t}}_n}{\partial\rho_e}=\sum_{j\ge i}\Bigg[\int_{\tau_{l_{j-1}}}^{\tau_{l_j}}\Bigg[{}^{l_i}_{l_j}\mathfrak{B}_n\mathbf{R}_n^T\frac{\partial\mathbf{T}_{l_j}}{\partial\rho_e}+\boldsymbol{\lambda}_{l_j}^T\frac{\partial}{\partial\rho_e}(\mathbf{C}_{l_j}\dot{\mathbf{T}}_{l_j}+\mathbf{K}_{l_j}\mathbf{T}_{l_j}-\mathbf{Q}_{l_j})\Bigg]dt\Bigg]. \tag{A.15}$$

Since, we are free to choose $\boldsymbol{\lambda}_{l_j}(t)$ values, therefore, we choose $\boldsymbol{\lambda}_{l_j}(t)=\mathbf{0}$, if $\tau_{l_{j-1}} \le t < \tau^{\mathfrak{h}}_{l_j}+\Delta\tau^{l_i}_{l_j}$. This will ensure no contribution to the sensitivities in the range $\tau_{l_{j-1}} \le t < \tau^{\mathfrak{h}}_{l_j}+\Delta\tau^{l_i}_{l_j}$. Moreover, $\mathbf{Q}_{l_j}=\mathbf{0}$, if $\tau^{\mathfrak{h}}_{l_j}+\Delta\tau^{l_i}_{l_j} \le t < \tau_{l_j}$, thus the term corresponding to $\mathbf{Q}_{l_j}$ will vanish. With these considerations and expanding the above equation will result in as follows

$$\frac{\partial \tilde{\mathfrak{t}}_n}{\partial \rho_e} = \sum_{j\geq i} \left[\int_{\tau_{l_{j-1}}}^{\tau_{l_j}} \left[{}^{l_i}_{l_j}\mathfrak{B}_n \mathbf{R}_n^T \frac{\partial \mathbf{T}_{l_j}}{\partial \rho_e} + \boldsymbol{\lambda}_{l_j}^T \mathbf{C}_{l_j} \frac{\partial \dot{\mathbf{T}}_{l_j}}{\partial \rho_e} + \boldsymbol{\lambda}_{l_j}^T \frac{\partial \mathbf{C}_{l_j}}{\partial \rho_e} \dot{\mathbf{T}}_{l_j} + \boldsymbol{\lambda}_{l_j}^T \frac{\partial \mathbf{K}_{l_j}}{\partial \rho_e} \mathbf{T}_{l_j} + \boldsymbol{\lambda}_{l_j}^T \mathbf{K}_{l_j} \frac{\partial \mathbf{T}_{l_j}}{\partial \rho_e} \right] dt \right]. \tag{A.16}$$

Now, applying the integration by parts for the term $\boldsymbol{\lambda}_{l_j}^T \mathbf{C}_{l_j} \frac{\partial \dot{\mathbf{T}}_{l_j}}{\partial \rho_e}$, to eliminate the term $\frac{\partial \dot{\mathbf{T}}_{l_j}}{\partial \rho_e}$ we get as follows

$$\int_{\tau_{l_{j-1}}}^{\tau_{l_j}} \left[\boldsymbol{\lambda}_{l_j}^T \mathbf{C}_{l_j} \frac{\partial \dot{\mathbf{T}}_{l_j}}{\partial \rho_e} \right] dt = \left[\boldsymbol{\lambda}_{l_j}^T \mathbf{C}_{l_j} \frac{\partial \mathbf{T}_{l_j}}{\partial \rho_e} \right]_{t=\tau_{l_j}} - \left[\boldsymbol{\lambda}_{l_j}^T \mathbf{C}_{l_j} \frac{\partial \mathbf{T}_{l_j}}{\partial \rho_e} \right]_{t=\tau_{l_{j-1}}} - \int_{\tau_{l_{j-1}}}^{\tau_{l_j}} \left[\dot{\boldsymbol{\lambda}}_{l_j}^T \mathbf{C}_{l_j} \frac{\partial \mathbf{T}_{l_j}}{\partial \rho_e} \right] dt. \tag{A.17}$$

Since, we assume that the $\boldsymbol{\lambda}_{l_j}(t) = \mathbf{0}$, for $\tau_{l_{j-1}} \leq t < \tau_{l_j}^{\mathfrak{h}} + \Delta\tau_{l_j}^{l_i}$, therefore, $\left[\boldsymbol{\lambda}_{l_j}^T \mathbf{C}_{l_j} \frac{\partial \mathbf{T}_{l_j}}{\partial \rho_e} \right]_{t=\tau_{l_{j-1}}} = \mathbf{0}$. Also, during the manufacturing process we assume that the part cools completely, therefore, $\left. \frac{\partial \mathbf{T}_{l_j}}{\partial \rho_e} \right|_{t=\tau_{l_j}} = \mathbf{0}$. Consequently, $\left[\boldsymbol{\lambda}_{l_j}^T \mathbf{C}_{l_j} \frac{\partial \mathbf{T}_{l_j}}{\partial \rho_e} \right]_{t=\tau_{l_j}} = \mathbf{0}$. Therefore, we are free to choose any $\boldsymbol{\lambda}_{l_j}$ and hence, we choose $\boldsymbol{\lambda}_{l_j}(t = \tau_{l_j}) = \mathbf{0}$. Moreover, if the condition is not satisfied $\left. \frac{\partial \mathbf{T}_{l_j}}{\partial \rho_e} \right|_{t=\tau_{l_j}} = \mathbf{0}$, then $\boldsymbol{\lambda}_{l_j}(t = \tau_{l_j}) = \mathbf{0}$ can be considered and this condition will work as initial condition to calculate complete $\boldsymbol{\lambda}_{l_j}(t)$. In both conditions, we can write as follows

$$\int_{\tau_{l_{j-1}}}^{\tau_{l_j}} \left[\boldsymbol{\lambda}_{l_j}^T \mathbf{C}_{l_j} \frac{\partial \dot{\mathbf{T}}_{l_j}}{\partial \rho_e} \right] dt = - \int_{\tau_{l_{j-1}}}^{\tau_{l_j}} \left[\dot{\boldsymbol{\lambda}}_{l_j}^T \mathbf{C}_{l_j} \frac{\partial \mathbf{T}_{l_j}}{\partial \rho_e} \right] dt. \tag{A.18}$$

Substituting, the above term in Eq. (A.16) we get

$$\frac{\partial \tilde{\mathfrak{t}}_n}{\partial \rho_e} = \sum_{j\geq i} \left[\int_{\tau_{l_{j-1}}}^{\tau_{l_j}} \left[{}^{l_i}_{l_j}\mathfrak{B}_n \mathbf{R}_n^T \frac{\partial \mathbf{T}_{l_j}}{\partial \rho_e} - \dot{\boldsymbol{\lambda}}_{l_j}^T \mathbf{C}_{l_j} \frac{\partial \mathbf{T}_{l_j}}{\partial \rho_e} + \boldsymbol{\lambda}_{l_j}^T \frac{\partial \mathbf{C}_{l_j}}{\partial \rho_e} \dot{\mathbf{T}}_{l_j} + \boldsymbol{\lambda}_{l_j}^T \frac{\partial \mathbf{K}_{l_j}}{\partial \rho_e} \mathbf{T}_{l_j} + \boldsymbol{\lambda}_{l_j}^T \mathbf{K}_{l_j} \frac{\partial \mathbf{T}_{l_j}}{\partial \rho_e} \right] dt \right]. \tag{A.19}$$

Now, collecting the contributions with term $\frac{\partial \mathbf{T}_{l_j}}{\partial \rho_e}$ we get

$$\frac{\partial \tilde{\mathfrak{t}}_n}{\partial \rho_e} = \sum_{j\geq i} \left[\int_{\tau_{l_{j-1}}}^{\tau_{l_j}} \left[\left\{ {}^{l_i}_{l_j}\mathfrak{B}_n \mathbf{R}_n^T - \dot{\boldsymbol{\lambda}}_{l_j}^T \mathbf{C}_{l_j} + \boldsymbol{\lambda}_{l_j}^T \mathbf{K}_{l_j} \right\} \frac{\partial \mathbf{T}_{l_j}}{\partial \rho_e} + \boldsymbol{\lambda}_{l_j}^T \frac{\partial \mathbf{C}_{l_j}}{\partial \rho_e} \dot{\mathbf{T}}_{l_j} + \boldsymbol{\lambda}_{l_j}^T \frac{\partial \mathbf{K}_{l_j}}{\partial \rho_e} \mathbf{T}_{l_j} \right] dt \right]. \tag{A.20}$$

The following set of adjoint equations can be solved to obtain the Lagrange multiplier values such that the term in the brackets always vanishes.

$$\mathbf{C}_{l_j} \dot{\boldsymbol{\lambda}}_{l_j} - \mathbf{K}_{l_j} \boldsymbol{\lambda}_{l_j} = {}^{l_i}_{l_j}\mathfrak{B}_n \mathbf{R}_n. \tag{A.21}$$

Subsequently, the design sensitivity of $\tilde{\mathfrak{t}}_n$ is given as follows:

$$\frac{\partial \tilde{\mathfrak{t}}_n}{\partial \rho_e} = \sum_{j\geq i} \left[\int_{\tau_{l_{j-1}}}^{\tau_{l_j}} \left[\boldsymbol{\lambda}_{l_j}^T \frac{\partial \mathbf{C}_{l_j}}{\partial \rho_e} \dot{\mathbf{T}}_{l_j} + \boldsymbol{\lambda}_{l_j}^T \frac{\partial \mathbf{K}_{l_j}}{\partial \rho_e} \mathbf{T}_{l_j} \right] dt \right]. \tag{A.22}$$

References

[1] T. DebRoy, H. Wei, J. Zuback, T. Mukherjee, J. Elmer, J. Milewski, A.M. Beese, A. d. Wilson-Heid, A. De, W. Zhang, Additive manufacturing of metallic components–process, structure and properties, Prog. Mater. Sci. 92 (2018) 112–224.

[2] J. Liu, A.T. Gaynor, S. Chen, Z. Kang, K. Suresh, A. Takezawa, L. Li, J. Kato, J. Tang, C.C. Wang, et al., Current and future trends in topology optimization for additive manufacturing, Struct. Multidiscip. Optim. 57 (6) (2018) 2457–2483.

[3] S. Kou, Welding Metallurgy, John Wiley & Sons, 2003.

[4] D. Kong, C. Dong, X. Ni, L. Zhang, X. Li, Cellular size dependence on the strength of additively manufactured austenitic stainless steel, Mater. Lett. 279 (2020) 128524.

[5] P. Delroisse, P.J. Jacques, E. Maire, O. Rigo, A. Simar, Effect of strut orientation on the microstructure heterogeneities in alsi10mg lattices processed by selective laser melting, Scr. Mater. 141 (2017) 32–35.

[6] Y. Zhao, Y. Chen, Z. Wang, J. Ye, W. Zhao, Mechanical properties, microstructural characteristics and heat treatment effects of waam stainless-steel plate material, J. Build. Eng. (2023) 106988.

[7] Y.T. Ang, S.L. Sing, J.C.W. Lim, Process study for directed energy deposition of 316l stainless steel with tib2 metal matrix composites, Mater. Sci. Addit. Manuf. 1 (2) (2022) 13.

[8] P. Kyvelou, H. Slack, D.D. Mountanou, M.A. Wadee, T.B. Britton, C. Buchanan, L. Gardner, Mechanical and microstructural testing of wire and arc additively manufactured sheet material, Mater. Des. 192 (2020) 108675.

[9] W.D. Callister Jr, D.G. Rethwisch, Fundamentals of Materials Science and Engineering: an Integrated Approach, John Wiley & Sons, 2020.

[10] W. Xu, M. Brandt, S. Sun, J. Elambasseril, Q. Liu, K. Latham, K. Xia, M. Qian, Additive manufacturing of strong and ductile Ti–6Al–4V by selective laser melting via in situ martensite decomposition, Acta Mater. 85 (2015) 74–84.

[11] S. Kelly, S. Kampe, Microstructural evolution in laser-deposited multilayer Ti-6Al-4V builds: part i. microstructural characterization, Metall. Mater. Trans. A 35 (6) (2004) 1861–1867.

[12] S. Kelly, S. Kampe, Microstructural evolution in laser-deposited multilayer ti-6al-4v builds: part ii. thermal modeling, Metall. Mater. Trans. A 35 (2004) 1869–1879.

[13] Y. Tian, D. McAllister, H. Colijn, M. Mills, D. Farson, M. Nordin, S. Babu, Rationalization of microstructure heterogeneity in INCONEL 718 builds made by the direct laser additive manufacturing process, Metall. Mater. Trans. A 45 (10) (2014) 4470–4483.

[14] P.H.G. Dornelas, J. da Cruz Payão Filho, F.W.C. Farias, V.H.P.M. e Oliveira, D. de Oliveira Moraes, P.Z. Júnior, Fem-thermodynamic simulation methodology to predict the influence of t8/5 on the coarse grain heat-affected zone of a Cr-Mo low-alloy steel pipe, J. Manuf. Process. 60 (2020) 520–529.

[15] T.A. Rodrigues, V. Duarte, J.A. Avila, T.G. Santos, R. Miranda, J. Oliveira, Wire and arc additive manufacturing of HSLA steel: effect of thermal cycles on microstructure and mechanical properties, Addit. Manuf. 27 (2019) 440–450.

[16] U. Reisgen, R. Sharma, S. Mann, L. Oster, Increasing the manufacturing efficiency of WAAM by advanced cooling strategies, Weld. World 64 (8) (2020) 1409–1416.

[17] Y. Shi, Z. Han, Effect of weld thermal cycle on microstructure and fracture toughness of simulated heat-affected zone for a 800 mpa grade high strength low alloy steel, J. Mater. Process. Technol. 207 (1–3) (2008) 30–39.

[18] V. Mishra, A. Babu, R. Schreurs, K. Wu, M. Hermans, C. Ayas, Microstructure estimation and validation of er110s-g steel structures produced by wire and arc additive manufacturing, J. Mater. Res. Technol. (2023).

[19] S. Wu, Y. Zhang, S. Liu, Topology optimization for minimizing the maximum temperature of transient heat conduction structure, Struct. Multidiscip. Optim. 60 (1) (2019) 69–82.

[20] S. Wu, Y. Zhang, S. Liu, Transient thermal dissipation efficiency based method for topology optimization of transient heat conduction structures, Int. J. Heat Mass Transf. 170 (2021) 121004.

[21] L. Gavard, H. Bhadeshia, D. MacKay, S. Suzuki, Bayesian neural network model for austenite formation in steels, Mater. Sci. Technol. 12 (6) (1996) 453–463.

[22] C. Huang, M. Soliman, K. Treutler, V. Wesling, K.-H. Spitzer, On the microstructure development under cyclic temperature conditions during waam of microalloyed steels, Metals 12 (11) (2022) 1913.

[23] R. Ranjan, C. Ayas, M. Langelaar, F. van Keulen, Fast detection of heat accumulation in powder bed fusion using computationally efficient thermal models, Materials 13 (20) (2020) 4576.

[24] R. Schreurs, Predicting thermal history, microstructure and hardness of wire arc additive manufactured parts, 2021.

[25] M.P. Bendsoe, O. Sigmund, Topology Optimization: Theory, Methods, and Applications, Springer Science & Business Media, 2013.

[26] T.E. Bruns, D.A. Tortorelli, Topology optimization of non-linear elastic structures and compliant mechanisms, Comput. Methods Appl. Mech. Eng. 190 (26–27) (2001) 3443–3459.

[27] K. Svanberg, The method of moving asymptotes—a new method for structural optimization, Int. J. Numer. Methods Eng. 24 (2) (1987) 359–373.
[28] M. Langelaar, An additive manufacturing filter for topology optimization of print-ready designs, Struct. Multidiscip. Optim. 55 (3) (2017) 871–883.
[29] E. van de Ven, R. Maas, C. Ayas, M. Langelaar, F. van Keulen, Continuous front propagation-based overhang control for topology optimization with additive manufacturing, Struct. Multidiscip. Optim. 57 (5) (2018) 2075–2091.
[30] K. Zhang, G. Cheng, L. Xu, Topology optimization considering overhang constraint in additive manufacturing, Comput. Struct. 212 (2019) 86–100.
[31] A.T. Gaynor, J.K. Guest, Topology optimization considering overhang constraints: eliminating sacrificial support material in additive manufacturing through design, Struct. Multidiscip. Optim. 54 (5) (2016) 1157–1172.
[32] T.J. Hughes, Unconditionally stable algorithms for nonlinear heat conduction, Comput. Methods Appl. Mech. Eng. 10 (2) (1977) 135–139.
[33] E. Pavlina, C. Van Tyne, Correlation of yield strength and tensile strength with hardness for steels, J. Mater. Eng. Perform. 17 (6) (2008) 888–893.